

Novel GaPtMnP Alloy Based Anodic Electrocatalyst with Excellent Catalytic Features for Direct Ethanol Fuel Cells

Young Soo Yoon, Padmini Basumatary, Mehmet Emin Kilic, Yoo Lim Cha, Kwang-Ryeol Lee, Dong-Joo Kim,* and Dimpul Konwar*

Although considerable effort has been devoted to developing bifunctional electrocatalysts with enhanced atomic utilization in ethanol fuel cells, significant progress in this field has been hindered by notable drawbacks of the electrocatalysts, such as low stability, poor activity, and inefficient repeatability for multiple startup and shutdown cycles. Considering these issues herein, a novel nanosized GaPtMnP alloy anchored on N-doped multiwall carbon nanotubes (MWCNTs) is developed. The average size of the spherical GaPtMnP alloy nanoparticles is ≈ 3.5 nm. The atomic structure and *d*-band shift of Pt in the GaPtMnP alloy are demonstrated using state-of-the-art density functional theory calculations. Cyclic voltammetry analysis revealed that GaPtMnP/N-MWCNT delivered high mass and specific activities of $9.16 \text{ A mg}_{\text{Pt}}^{-1}$ and 10.4 mA cm^{-2} , respectively, in $0.3 \text{ M H}_2\text{SO}_4 + 0.5 \text{ M ethanol}$, values that are ≈ 13 - and 8 -fold higher than the corresponding values for Pt/C. In addition, it exhibits long-term stability and durability even after 3000 cycles. A single cell based on the GaPtMnP/N-MWCNT anodic electrocatalyst exhibits a peak power density of 86.64 mW cm^{-2} , which is approximately fourfold higher than that of Pt/C at 70°C . Furthermore, the performance of a fuel cell comprising the GaPtMnP/N-MWCNT catalyst remained constant even after multiple startup–shutdown cycles.

and ease of transportation, storage, and handling.^[1,2] Another advantage of DEFCs is the easy availability of ethanol. Furthermore, ethanol can be produced from abundantly available agricultural raw materials, such as sugarcane and corn.^[3,4] Therefore, the demand for DEFCs as a renewable power source generator has increased over the past few years. However, to improve the performance of DEFCs, the complete oxidation of ethanol is necessary, which involves a complex C–C bond dissociation mechanism. Unfortunately, C–C bond dissociation induces the formation of CH_{ads} and CO_{ads} species, leading to the production of CO_2 , which subsequently poisons the electrocatalyst.^[5,6] This reduces the stability and durability of DEFCs, thus deteriorating their performance. Therefore, the development of a robust and durable anodic electrocatalyst capable of effectively oxidizing ethanol in DEFCs remains a challenge.

Platinum group nanomaterials are the most widely implemented catalysts

in DEFCs, especially for the anodic ethanol oxidation reaction (EOR), owing to their excellent performances.^[7] However, the large-scale application of pure Pt-based electrocatalysts is limited by several drawbacks, including the scarcity of Pt, high Pt loading, high cost, poor stability, and poisoning. Two strategies can be implemented to overcome these limitations. The first strategy is to reduce Pt usage by alloying it with inexpensive transition metals.^[8] The second is to realize the high atomic-level utilization of Pt to achieve enhanced catalytic performances.^[9]

Alloying Pt with less-expensive and abundant metals, such as Ni, Co, Cu, Mn, and Fe, can enhance its catalytic activity through electronic effects and the lattice strain derived from distinct electron orbital hybridizations and atomic radii.^[10,11] In general, Pt-based binary catalysts, such as PtNi,^[12] PtCo,^[13] PtMn,^[14] GaPt,^[15] and PtCu^[16] are considered promising electrocatalysts owing to their bifunctional and strain effects, which readily tune their electronic properties, thereby protecting the active sites during potential cycling.^[16] Although Mn is highly effective for alloying with Pt; its characteristics in acidic media and in ethanol oxidation are less explored.^[17,18] Kang and Murray illustrated that alloying Pt with Mn (nanocubic catalyst) can reduce the cost as well as generate more active sites within the catalyst in acidic media.^[19] They prepared an alloy with a Pt:Mn


1. Introduction

Renewable energy generators, such as direct ethanol fuel cells (DEFCs), are considered a propitious power source both stationary and portable applications. DEFCs have several advantages over hydrogen fuel cells, such as a high specific energy density (8.03 kWh Kg^{-1}), cost efficiency, low hazard concerns,

Y. S. Yoon, P. Basumatary, D. Konwar
Department of Materials Science and Engineering
Gachon University
Bokjung-dong, Seongnam-si, Gyeonggi-Do 1342, Republic of Korea
E-mail: dkonwar@gachon.ac.kr

M. E. Kilic, K.-R. Lee
Center for Computational Science Research
KIST
Seoul 02792, Republic of Korea

Y. L. Cha, D.-J. Kim
Materials Research and Education Center
Auburn University
Auburn, AL 36849, USA
E-mail: kimdon2@auburn.edu

 The ORCID identification number(s) for the author(s) of this article can be found under <https://doi.org/10.1002/adfm.202111272>.

DOI: 10.1002/adfm.202111272

ratio of 3:1 for their nanocubic and spherical structured catalysts and achieved superior electrocatalytic activity toward the methanol oxidation reaction than the spherical PtMn catalyst. Meanwhile, Rodríguez et al. theoretically and experimentally studied Pt–Mn alloys and employed them for methanol oxidation. The electrocatalyst's performance was enhanced when the amount of Mn in Pt alloy nanoparticles was up to 40 at%, and it decreased with further increase in Mn percentage.^[20] Du et al. developed a novel PtMn (nanowires with a diameter of ≈ 1 nm) catalyst and achieved enhanced alcohol oxidation compared to Pt/C.^[14]

Gao et al. illustrated how unconventional hybridization of p-d orbitals of PtGa alloy boosted the oxygen reduction reaction (ORR) and minimized the influence of CO poisoning.^[15] Lim et al. obtained enhanced catalytic activity using GaPt₃ (1:3 ratio) toward the hydrogen evolution reaction (HER) along with a very low overpotential.^[21] However, compared to binary electrocatalysts, ternary Pt-based alloys or composites show improved tunability and catalytic activity owing to the synergic effect of their constituents, which endows the electrocatalysts with new properties for further stabilization.^[11] For example, PtPdCu nanodendrite alloys,^[22] PtIrNi alloy nanoparticles,^[23] GaPtNi octahedral nanoparticles,^[24] GaPtCe,^[25] and PtNiM (M = Rh, Os, and Ir) nanowires^[26] have demonstrated outstanding activity and excellent stability. Cho et al. elucidated that although PtNi can exhibit better electrocatalytic activity the long-term operation of a typical fuel cell leads to the dissolution of Ni atoms into the electrolyte and eventual degradation of the fuel cell.^[24] They further confirmed that the addition of Ga atoms to PtNi not only increases the catalytic activity, but also prevents agglomeration and dealloying (Ni atom dissolving) of PtNi. Meanwhile, Li et al. synthesized lavender-like nanowires of Ga-doped Pt₃Co with enhanced catalytic activity and durability for alcohol (methanol and ethanol) oxidation.^[27] Furthermore, Bauer et al. reported that the addition of Ga to Pt can improve its electrochemical performance because Ga⁺ species can enhance the catalytic activity of isolated Pt atoms, and assist the depleted Pt such that it reappears on the surface via adsorption.^[28] Moreover, the introduction of heteroatoms (like P, N, and S) in a catalyst is an efficient strategy for modifying its electronic and geometric structures, and hence, improving its durability and activity. An electrocatalyst doped with P generates abundant valence electrons, which can tune the electronic state of noble metals, resulting in enhanced catalytic properties.^[29]

Various P-doped Pt-based composites have been studied, including PtP,^[30] PtP₂,^[31] PtNiP,^[32] PtFe₂P,^[33] and PtTeP,^[34] owing to their remarkable catalytic activity and stability. Furthermore, the alloying of Pt with P composites can decrease the adsorption strength of CO. This is because P doping can lower the d-band center of Pt.^[32] Lv et al. demonstrated the role of P in improving the catalytic performance of PdCu nanowires.^[29] Their P-doped PdCu nanowires exhibited an excellent EOR performance with a mass activity of 6.67 A mg_{Pd}⁻¹, which was 9.3-fold higher than that of Pd nanoparticles (0.71 A mg_{Pd}⁻¹). Ji et al. developed a P-doped Ag@NC composite and achieved improved HER performance with excellent stability for 85 h.^[35] Shin et al. prepared a novel Fe_xNi_{2-x}P catalyst to effectively promote the HER in an acidic medium. This catalyst exhibited a low Tafel slope of 65 mV dec⁻¹ and an enhanced current density

of 0.37 mA cm⁻².^[36] Lai et al. designed P–CoO core@shell microspheres and attained a low overpotential, excellent stability toward the HER, and high capacitance.^[37] Li et al. investigated the effect of P doping on Co₉S₈@CS for zinc–air batteries and the oxygen evolution reaction (OER).^[38] This P-doped Co₉S₈@CS catalyst was highly promising for application in the oxygen evolution reaction (OER) and zinc–air batteries. Furthermore, Guo et al. demonstrated that the phosphorization of Pt improves the catalytic activity of Pt₂P catalyst toward the oxygen reduction reaction (ORR).^[39] Motivated by the aforementioned achievements, we envisaged a P-doped electrocatalyst for enhanced ethanol oxidation at low temperature.

The second strategy for enhancing the catalytic activity of Pt-based electrocatalysts is the phase design of nanomaterials with small particle sizes and shape-controlled composites. The catalysts obtained using this approach showed improved Pt atom utilization efficiency compared to their bulk counterparts.^[40] Composites with unique morphologies, such as nanoparticles (sized 2–10 nm), nanocubes, tripod structures, nanorods, cage-bell structures, and porous structures have been studied, because a large surface area can be generated by tuning their properties, which enhances adsorption at the edge and corner atoms, facilitating the activation of reactant molecules.^[41,42] Furthermore, the strain, interfacial, crystal, and composition effects of the nanoparticles can significantly contribute toward decreasing the reaction barrier and can enhance the electrocatalytic activity.^[43]

The use of carbon as a support material significantly affects the activity and durability of the catalyst in fuel cells.^[44] Remarkable advancement has been achieved in the development of electrocatalysts with uniformly dispersed metal, metal-oxide, and alloy nanoparticles on a carbon support. However, carbon undergoes rapid corrosion during multiple startup/shutdown processes at high potentials and in fuel-deficient conditions.^[45,46] This limits the application of carbon supports in fuel cell electrocatalysts. The corrosion or degradation of carbon results in the detachment and agglomeration of catalyst nanoparticles and reduces OH adsorption because of the proximity effect, thereby reducing the oxidation of CO_{ads} and compromising the long-term durability of the catalyst.^[44,47] Furthermore, carbon corrosion increases the hydrophilicity of the surface, which results in flooding of the active sites in the electrocatalyst layer. Therefore, the surface functionalization of graphene, carbon black, and carbon nanotubes (CNTs) is performed to enhance fuel oxidation in fuel cells. Multiwall CNTs (MWCNTs) are a promising support material because they exhibit high conductivity within metal or alloy nanoparticle electrocatalysts.^[48] Oxidized MWCNTs consist of numerous hydrophilic functional groups. These groups are present on the surface of MWCNTs and facilitate the uniform dispersion and deposition of nanoparticles. However, oxygen-rich functional groups can lead to the development of defective MWCNTs, which undergo gradual corrosion.^[49] In this regard, it has been reported that defective MWCNTs generated by doping with P, S, B, and N do not degrade the support, but improve the dispersion and catalytic efficiency of alloy nanoparticles. Furthermore, N-doped MWCNTs show improved conductivity and π – π bond interactions due to the electronic rearrangement induced by the external electrons of N atoms.^[50] Thus, the application

of N-doped MWCNTs as a support material for electrocatalyst nanoparticles is beneficial for achieving long-term stability and improved catalytic activity.

Herein, ultrasmall spherical GaPtMnP alloy nanoparticles with increased atomic exposure were anchored onto a N-doped MWCNT support. A GaPtMnP/N-MWCNT catalyst was prepared via a simple two-step hydrothermal synthesis method. For comparison, GaPtP/N-MWCNT, PtMnP/N-MWCNT, and PtP/N-MWCNT were prepared and evaluated. GaPtMnP/N-MWCNT exhibited promising electrocatalytic activity for the EOR. To the best of our knowledge, this type of novel fuel cell electrocatalyst has not been reported to date. Furthermore, the GaPtMnP/N-MWCNT electrocatalyst exhibited promising catalytic activity toward the EOR in a DEFC.

2. Results and Discussion

2.1. Characterization of Nanocomposite Materials

The preparation of the GaPtMnP/N-MWCNT nanocomposite catalyst involved a simple two-step hydrothermal procedure, as schematically illustrated in Figure 1A. The first step involved the preparation of N-doped MWCNTs. In the second step, the metal precursors were added to the N-doped MWCNTs and the mixture was subjected to a hydrothermal reaction at 160 °C for 5 h. Thus, the GaPtMnP alloy nanoparticles were formed and anchored on the N-MWCNTs. GaPtMnP/N-MWCNT is a novel nanocomposite electrocatalyst being studied herein for the EOR and applied to a DEFC for the very first time.

The crystallinity and phase structures of the alloy nanocomposites were determined by XRD, and are shown in Figure 1B and Figure S1, Supporting Information. GaPtMnP/N-MWCNT

showed reflection peaks at $\approx 40.4^\circ$, $\approx 46.6^\circ$, $\approx 68.1^\circ$, and $\approx 82.1^\circ$ corresponding to the (111), (200), (220), and (311) lattice planes of the Pt structure, respectively, within a face-centered cubic structure (JCPDS No: 87-0646).^[51] The diffraction peaks of GaPtMnP/N-MWCNT were broad and shifted slightly toward a higher 2θ value compared with those of commercial Pt/C, indicating that Ga, Mn, and P were incorporated into the Pt face-centered cubic structure. Diffraction peaks related to the existence of any secondary phases were absent. The GaPtMnP alloy crystallized in the Fm-3m space group with a d-spacing of 0.235 nm. On the other hand, the diffraction peak at 26.3° was associated with the (002) plane, which resembles the graphitic (hexagonal) carbon structure of the MWCNTs (JCPDS No: 41-1487).^[52,53] The average crystallite size of Pt in commercial Pt/C is 5 nm, whereas that of the GaPtMnP alloy was ≈ 3.8 nm. Thus, Pt alloy formation was further confirmed by the contraction of the lattice. A similar Pt peak shift was observed for GaPtP/N-MWCNT, PtMnP/N-MWCNT, and PtP/N-MWCNT.

The pore volumes and Brunauer–Emmett–Teller (BET) specific surface areas of the alloy nanocomposite catalysts were determined after obtaining their nitrogen adsorption–desorption isotherms. The isotherm curves of GaPtMnP/N-MWCNT and PtP/N-MWCNT are shown in Figure 1C. GaPtMnP/N-MWCNT exhibited a larger specific surface area and a higher pore volume ($223.64 \text{ m}^2 \text{ g}^{-1}$ and $0.098 \text{ cm}^3 \text{ g}^{-1}$, respectively) than PtP/N-MWCNT ($51.81 \text{ m}^2 \text{ g}^{-1}$ and $0.011 \text{ cm}^3 \text{ g}^{-1}$). In addition, GaPtP/N-MWCNT and PtMnP/N-MWCNT exhibited specific surface areas of 139.27 and $139.16 \text{ m}^2 \text{ g}^{-1}$, respectively (Figure S2, Supporting Information). The pore size distribution plots of the catalysts were acquired from their Barrett–Joyner–Halenda (BJH) isotherm data. From Figure 1D, it can be ascertained that the structure of GaPtMnP/N-MWCNT is mesoporous. The average pore size (width) of GaPtMnP/N-MWCNT was

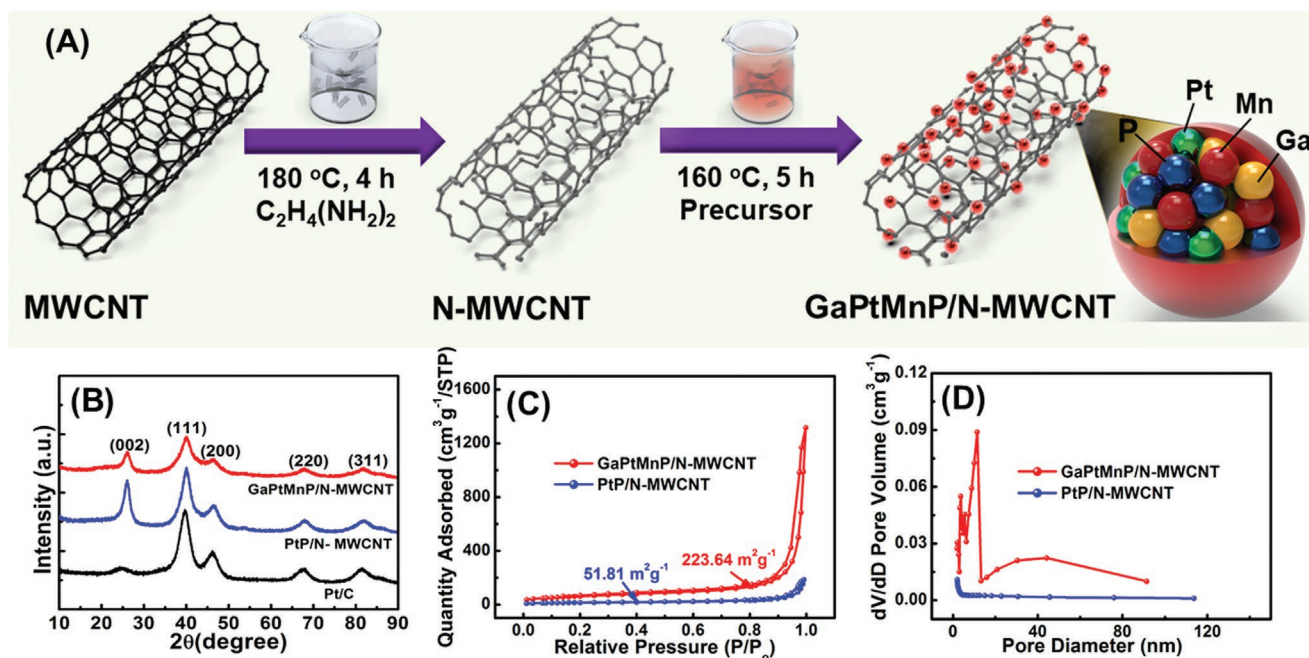


Figure 1. A) Schematic for the preparation of the GaPtMnP/N-MWCNT nanocomposite. B) XRD patterns of GaPtMnP/N-MWCNT, PtP/N-MWCNT, and Pt/C. C) Nitrogen adsorption/desorption isotherms of GaPtMnP/N-MWCNT and PtP/N-MWCNT and D) their pore size distributions.

27.33 nm, while that of PtP/N-MWCNT was 15.51 nm. The higher pore volume and larger specific surface area of the GaPtMnP/N-MWCNT nanocomposite can be attributed to the incorporation of Ga, Mn, and P into Pt, which acted as promoters or co-catalysts and contributed to the generation of new active sites. The larger specific surface area of the catalyst not only generated highly accessible active sites, but also improved the contact between the electrolyte and active material sites.^[54] This resulted in the shortening of the electron/ion transfer path during the electrochemical processes, thereby improving the electrocatalytic activity.^[11,55]

The morphologies of the as-synthesized catalysts were examined using scanning electron microscopy (SEM) and high-resolution transmission electron microscopy (TEM) (HR-TEM). The SEM images of GaPtMnP/N-MWCNT, GaPtP/N-MWCNT, PtMnP/N-MWCNT, and PtP/N-MWCNT are shown in **Figure 2**. Ultrasmall GaPtMnP alloy nanoparticles were well-anchored on the N-doped MWCNT surface, thus forming a uniform thin coating over the N-MWCNTs. In addition, the energy-dispersive X-ray spectroscopy (EDS) results for GaPtMnP/N-MWCNT (Figure S3, Supporting Information) confirmed the elemental composition and respective content (weight percentage), as shown in Table S1, Supporting Information. The EDS mapping of O, N, and C of N-doped MWCNT is shown in Figure S4, Supporting Information. The N-doped MWCNTs (Figure S5A, Supporting Information) exhibited some wrinkled sites that could strongly adhere to the alloy nanoparticles, demonstrating the advantages of the simple hydrothermal treatment for synthesizing N-MWCNTs over the expensive arc discharge and chemical vapor deposition methods.^[56]

The catalysts were further investigated using HR-TEM and EDS mapping (**Figure 3**). The GaPtMnP alloy in the GaPtMnP/N-MWCNT catalyst exhibited spherical nanoparticles, which were well-anchored on the N-doped MWCNTs (Figure 3A). The corresponding nanoparticle size distribution pattern (≈ 1800 particles) is shown in Figure 3B; the average particle size of the alloy nanoparticles was ≈ 3.5 nm, as calculated using ImageJ software (USA). The TEM images and size distributions of GaPtP/N-MWCNT, PtMnP/N-MWCNT, and PtP/N-MWCNT are shown in Figure S5, Supporting Information. The average particle sizes of GaPtP/N-MWCNT, PtMnP/N-MWCNT, and PtP/N-MWCNT were ≈ 4 , 5, and 3 nm, respectively. The HR-TEM image shown in Figure 3E indicated crystal lattice spacing's of 0.24 and 0.35 nm, corresponding to the (111) plane of GaPtMnP nanoparticles and the (002) plane of carbon (MWCNT), respectively. The increased lattice spacing in GaPtMnP compared to the standard crystal lattice spacing of 0.226 nm for Pt (111) can be attributed to the co-doping/addition of Ga, Mn, and P atoms into the Pt lattice structure, thus confirming alloy formation.^[57,58] The selected area electron diffraction (SAED) pattern (Figure 3F) revealed the polycrystalline nature of GaPtMnP.^[21] The elemental mapping (Figure 3G–L) of the GaPtMnP/N-MWCNT nanocomposite catalyst confirmed the presence and distribution of Ga, Pt, Mn, and P along with that of O and N. In addition, the HAADF-STEM image and EDS mapping of GaPtP/N-MWCNT (Figure S5G,J, Supporting Information) confirmed the robust anchoring of GaPtP alloy nanoparticles on N-MWCNT.

The surface oxidation states and compositions of the as-prepared nanocomposite catalysts were examined using X-ray photoelectron spectroscopy (XPS) (**Figure 4**, and Figure S6 and

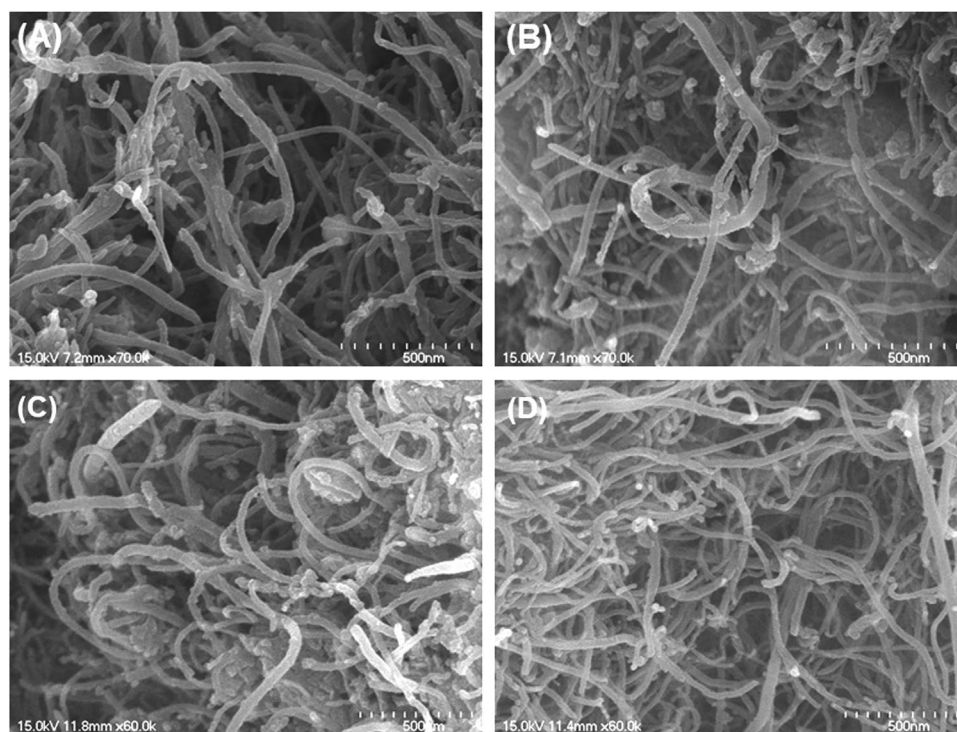


Figure 2. SEM images of A) GaPtMnP/N-MWCNT, B) GaPtP/N-MWCNT, C) PtMnP/N-MWCNT, and D) PtP/N-MWCNT.

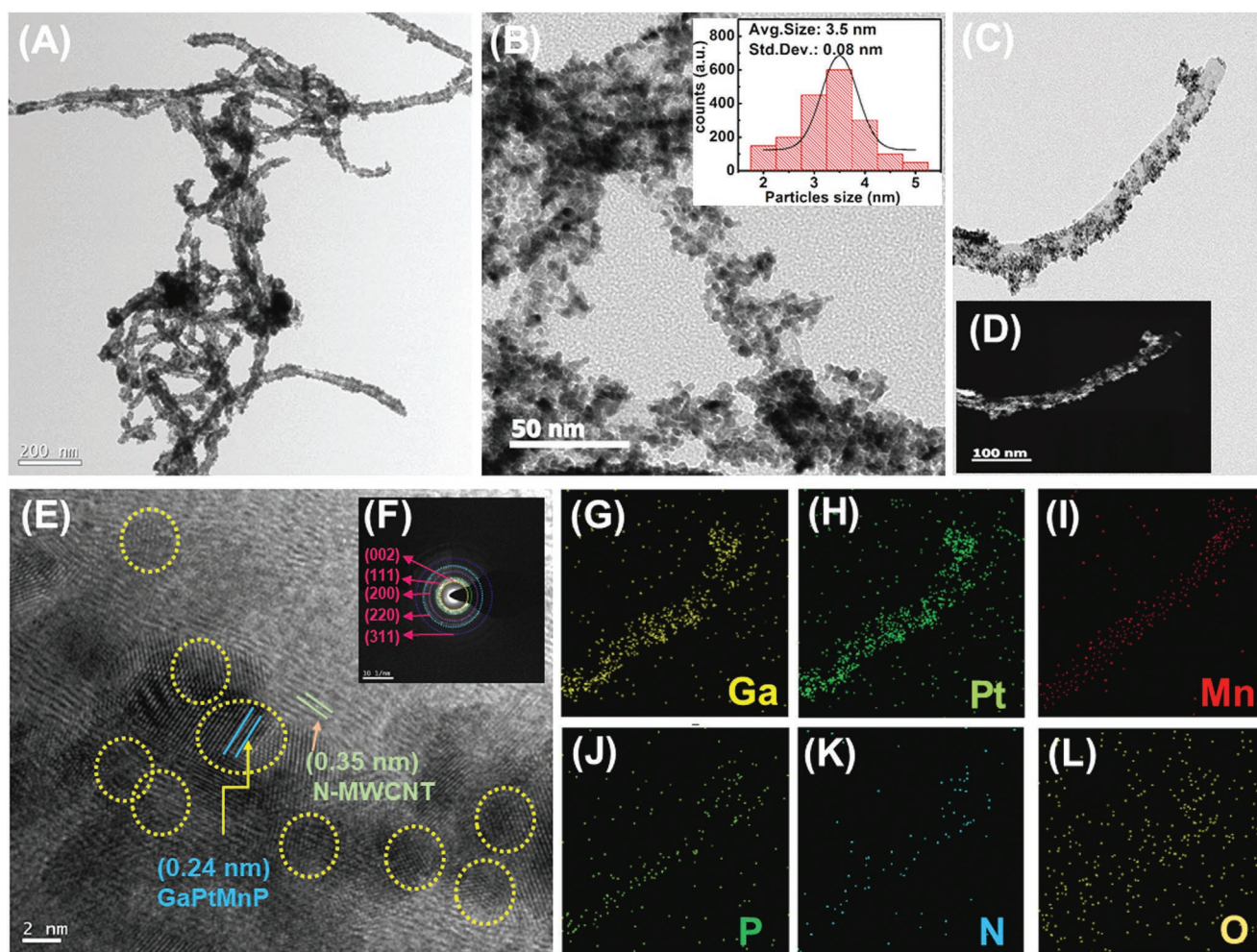


Figure 3. TEM images of A–C) GaPtMnP/N-MWCNT. D) HAADF-STEM image and E) HR-TEM image of GaPtMnP/N-MWCNT. F) SAED pattern and G–L) EDS mapping of GaPtMnP/N-MWCNT in (C).

Table ST2, Supporting Information). The survey scan XPS profile of GaPtMnP/N-MWCNTs (Figure 4A) confirmed the existence of Ga, Pt, Mn, P, O, and C (MWCNT). The N1s profile (Figure 4B) exhibited peaks at 399.3, 401.1, and 402.6 eV, which were ascribed to pyridinic N, pyrrolic/pyridone N, and graphitic N, respectively.^[59,60] The Ga 3d peaks (Figure 4C) indicated that Ga existed in metallic Ga⁰ and Ga³⁺ states (Ga₂O₃).^[24,27] The Ga2p peaks (Figure S7, Supporting Information) at 1118.4 and 1144.5 eV were also related to the Ga³⁺ state of gallium. The Pt4f profile (Figure 4D) displayed peaks at 71.4 (4f_{7/2}) and 74.1 eV (4f_{5/2}) corresponding to the metallic Pt⁰ state, while the other two distinguishable peaks at 72.3 (4f_{7/2}) and 75.4 eV (4f_{5/2}) could be attributed to the presence of Pt²⁺ (mainly in Pt(OH)₂, PtO₂, and PtO phases).^[61,62]

In the Mn2p profile (Figure 4E), the peak at 639.5 eV corresponds to metallic Mn species, while the peaks at 640.8 (2p_{3/2}), 652.6 (2p_{1/2}), 642.4 (2p_{3/2}), and 654.5 (2p_{1/2}) can be attributed to Mn²⁺ and Mn³⁺ oxidation states.^[63,64] Additionally, the peaks at 645.6 (2p_{3/2}) and 657.9 eV (2p_{1/2}) correspond to the Mn⁴⁺ state.^[65] In Figure 4F, the peaks at 129.1 and 130.4 eV can be attributed to the P2p_{3/2} and P2p_{1/2} levels of the metallic state (P⁰), respectively, while the peak at 132.6 eV corresponds to the P⁵⁺ state

(P₂O₅). The peaks located at 134.4, 136.5, and 137.7 eV were assigned to P–C, P–O–C, and P–O species, respectively.^[66,67] Furthermore, it is evident that the Pt4f peaks of GaPtMnP/N-MWCNT showed a positive shift (0.04 eV) compared to those of the pure metallic Pt species (Pt⁰).^[11] This is because alloying Pt with Ga, Mn, and P leads to a change in its electronic structure. Furthermore, this adjustment of the electronic structure of Pt in GaPtMnP/N-MWCNT can mitigate or disfavor the surface chemisorption of poisonous intermediate states, such as CO, CHO, and COOH, and accelerate the EOR.^[68] The XPS profiles and peak fitting of C1s and O1s of GaPtMnP/N-MWCNT are shown in Figure S8, Supporting Information, and their significance is illustrated in the Supporting Information. The inductively coupled plasma atomic emission spectroscopy (ICP-MS) data for GaPtMnP/N-MWCNT, GaPtP/N-MWCNT, PtMnP/N-MWCNT, and PtP/N-MWCNT are shown in Table ST3, Supporting Information. From the ICP-MS analysis, it was evident that the Ga, Pt, and Mn were present in the GaPtMnP/N-MWCNT in the ratio ≈1:3:1. The doping percentages of P obtained for GaPtMnP/N-MWCNT, GaPtP/N-MWCNT, PtMnP/N-MWCNT, and PtP/N-MWCNT were ≈4.07%, 4.41%, 4.04%, and 4.92%, respectively.

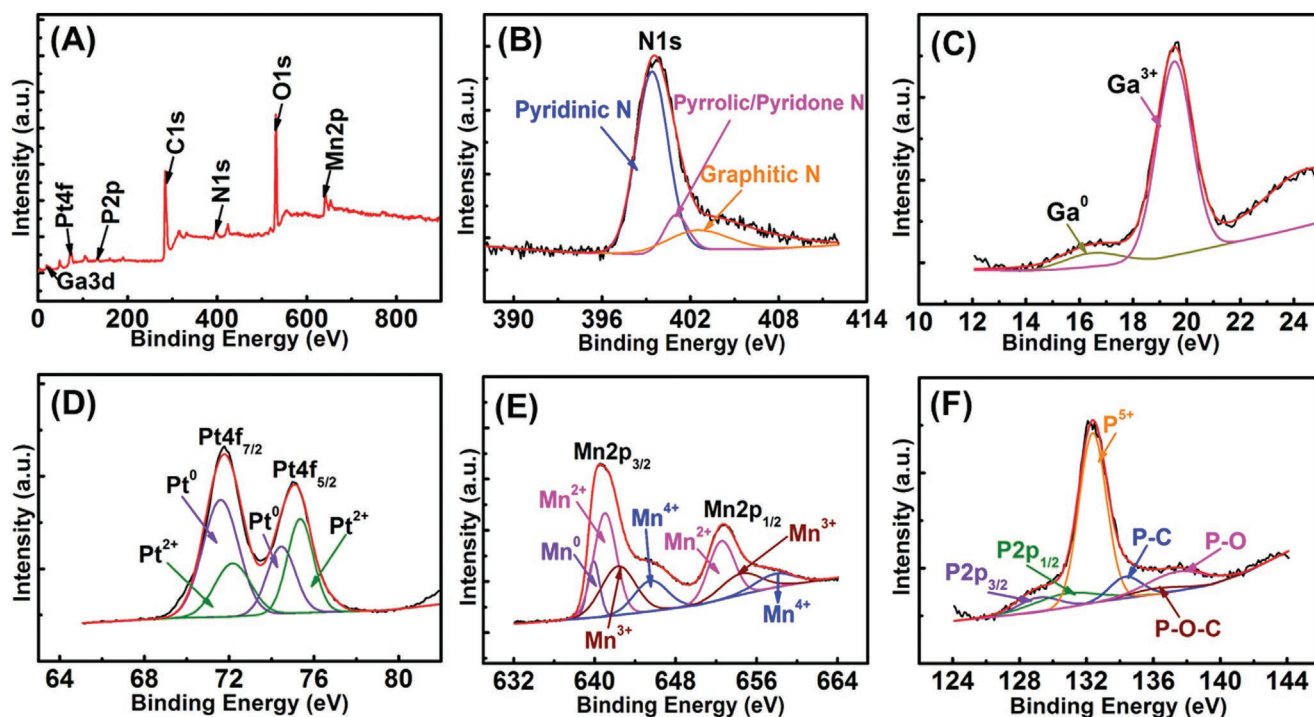


Figure 4. A) XPS survey profile of the GaPtMnP/N-MWCNT catalyst and corresponding peak fitting of B) N1s, C) Ga3d, D) Pt4f, E) Mn2p, and F) P2p.

2.2. Electrochemical Performance Analysis

Initially, the catalysts were examined in 0.3 M H_2SO_4 at a scan rate of 20 mV s^{-1} over the potential range of -0.2–1.0 V (versus Ag/AgCl), to determine their active electrochemical surface area (ECSA). Each catalyst showed distinct hydrogen adsorption–desorption peaks and oxidation/reduction features (Figure 5A). GaPtMnP/N-MWCNT ($\approx 1:3:1$ of Ga, Pt, and Mn) exhibited a larger ECSA (88.1 $\text{m}^2 \text{g}^{-1}$) than GaPtP/N-MWCNT (79.7 $\text{m}^2 \text{g}^{-1}$), PtMnP/N-MWCNT (70.8 $\text{m}^2 \text{g}^{-1}$), PtP/N-MWCNT (62.4 $\text{m}^2 \text{g}^{-1}$), and Pt/C (57.3 $\text{m}^2 \text{g}^{-1}$). For optimization of Pt, GaPtMnP/N-MWCNT was synthesized in two more ratios of Ga, Pt, and Mn: $\approx 1:2.4:1$ and $\approx 1:2:1$ and were further analyzed for the EOR. The catalyst with ($\approx 1:3:1$) ratio exhibited better catalytic activity than the other two catalysts, as is evident from Figure S9 and Table ST4, Supporting Information. Therefore, only the GaPtMnP/N-MWCNT catalyst with an elemental ratio of $\approx 1:3:1$ was explicitly illustrated in this report. The larger ECSA of GaPtMnP/N-MWCNT enables the accommodation of a higher number of accessible active sites, which contribute to enhancing the catalytic activity toward the EOR.^[11,68]

The electrochemical properties of the electrocatalysts were further investigated in a solution of 0.3 M H_2SO_4 + 0.5 M ethanol at a scan rate of 20 mV s^{-1} . The onset potential (Figure 5C) of GaPtMnP/N-MWCNT shifted toward the negative direction compared to that of the other catalysts, indicating that the EOR occurred readily on its surface with minimum energy loss. This also suggests that the doping of active Pt sites with several specific metals induces a more pronounced synergistic effect than doping with one or two metals.^[25]

The mass activity of GaPtMnP/N-MWCNT (9165.5 $\text{mA mg}^{-1}_{\text{Pt}}$) was ≈ 1.25 -, 1.76-, 4.57-, and 12.6-fold

higher than those of GaPtP/N-MWCNT (7278.2 $\text{mA mg}^{-1}_{\text{Pt}}$), PtMnP/N-MWCNT (5197.2 $\text{mA mg}^{-1}_{\text{Pt}}$), PtP/N-MWCNT (2004.2 $\text{mA mg}^{-1}_{\text{Pt}}$), and Pt/C (727.7 $\text{mA mg}^{-1}_{\text{Pt}}$), respectively. Moreover, GaPtMnP/N-MWCNT exhibited enhanced specific activity toward the EOR (10.4 mA cm^{-2}) compared with GaPtP/N-MWCNT (9.13 mA cm^{-2}), PtMnP/N-MWCNT (7.34 mA cm^{-2}), PtP/N-MWCNT (3.21 mA cm^{-2}), and Pt/C (1.26 mA cm^{-2}). This indicates that GaPtMnP/N-MWCNT showed excellent intrinsic activity (Figure 5E). Moreover, as indicated in Table 1, the GaPtMnP/N-MWCNT nanocomposite catalyst exhibited a substantially higher catalytic activity toward the EOR compared to previously reported Pt-based composite catalysts.

Next, the stability, durability, and catalytic efficiency of the catalysts were evaluated. Chronoamperometry (CA) measurements were performed at 0.4 V for 24 h, followed by cycling for 3000 consecutive cycles at a scan rate of 20 mV s^{-1} in 0.3 M H_2SO_4 + 0.5 M ethanol solution, under a N_2 -saturated atmosphere (Figure 5F and Figure S10, Supporting Information [initial 60 s data]). All the nanocomposite catalysts delivered a higher oxidation current than commercial Pt/C. This can be attributed to the following: 1) better interactions between the catalyst and the reaction interface, also referred to as electrical/charging double-layer activity; and 2) a higher abundance of active sites on the catalyst surface.^[76] The minimal decrease in the oxidation current observed in the final stage in Figure 5F indicates the formation of unwanted residues of intermediate species and by-products on the active sites of the catalysts, which were rapidly oxidized and automatically removed; this was followed by repeated cycling tests.^[55,77]

GaPtMnP/N-MWCNT exhibited a high oxidation current and excellent poisoning tolerance in acidic media, superior to those of the other catalysts investigated in this study. Furthermore,

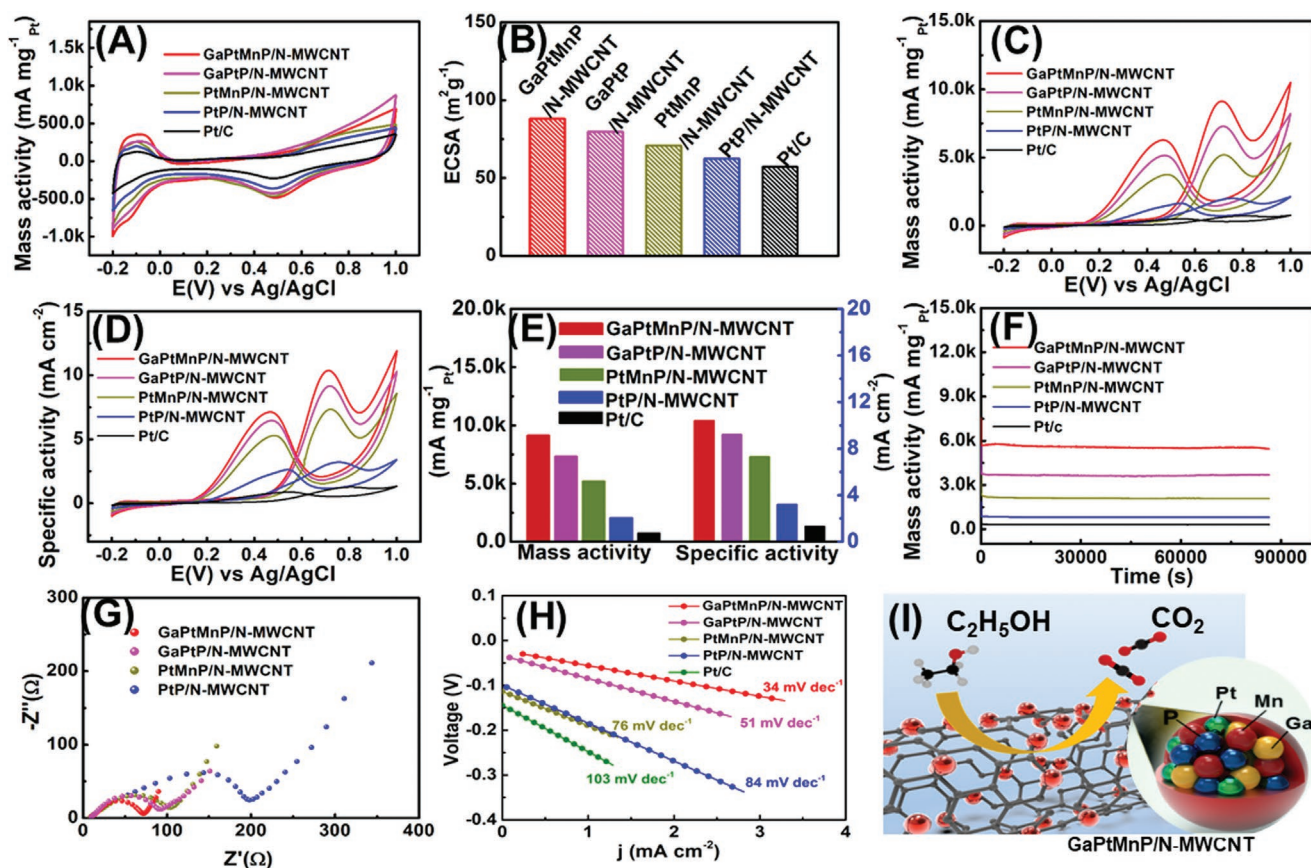


Figure 5. A) CV curves of the as-prepared catalysts at a scan rate of 20 mV s^{-1} in $0.3 \text{ M H}_2\text{SO}_4$ under nitrogen atmosphere. B) ECSA representation of the catalysts. C) Mass activity, D) specific activity in $0.3 \text{ M H}_2\text{SO}_4 + 0.5 \text{ M}$ ethanol, and E) their graphical comparison. F) Chronoamperometric measurements of the catalysts at 0.4 V for 24 h in a solution of $0.3 \text{ M H}_2\text{SO}_4$ and 0.5 M ethanol. G) Nyquist plots and H) Tafel plots of the catalysts. I) EOR mechanism on GaPtMnP/N-MWCNT.

catalyst degradation after 3000 cycles occurred to the lowest extent in the GaPtMnP/N-MWCNT nanocomposite (Figure S11, Supporting Information). After 3000 cycles, GaPtMnP/N-MWCNT retained 89.3% of its forward peak mass activity, while GaPtP/N-MWCNT, PtP/N-MWCNT, and Pt/C maintained 82.9%, 41.1%, and 30.2% of their forward mass activities, respectively.

To investigate the effect of the scan rate on the EOR activity of the catalysts, the CV curves of GaPtMnP/N-MWCNT and Pt/C were obtained at various potential scan rates in a $0.3 \text{ M H}_2\text{SO}_4 + 0.5 \text{ M}$ ethanol solution, and are presented in Figure S12, Supporting Information. The forward oxidation peaks for the EOR increased with increasing scan rate. The linear relationship between the forward anodic oxidation peak intensity and the square root of the potential scan rates suggests that the EOR occurring at the surface of the catalysts was controlled by charge and mass transport kinetics.^[48,54] GaPtMnP/N-MWCNT exhibited a higher slope (764.48) than Pt/C (41.21). This indicates that the rate-determining electron transfer step was faster in GaPtMnP/N-MWCNT.^[11] Furthermore, this enhancement in the electrocatalytic activity of GaPtMnP/N-MWCNT can be ascribed to the stress and electronic effects generated by Ga, Mn, and P doping. The uniform deposition of catalyst nanoparticles on N-MWCNTs and the small size of the spherical alloy nanoparticles also played a vital role in improving the overall

catalytic activity of GaPtMnP/N-MWCNT. The Nyquist plots of GaPtMnP/N-MWCNT, GaPtP/N-MWCNT, PtMnP/N-MWCNT, and PtP/N-MWCNT are shown in Figure 5G. GaPtMnP/N-MWCNT showed the lowest electron charge transfer resistance of the studied catalysts. The electron charge transfer resistance of the catalysts increased in the following order: GaPtMnP/N-MWCNT < GaPtP/N-MWCNT < PtMnP/N-MWCNT < PtP/N-MWCNT. This indicates that the EOR active sites in GaPtMnP/N-MWCNT were more conductive and consumed less energy, as further confirmed by the Tafel plot analysis (Figure 5H).^[54] The Tafel plots of the catalysts were determined from the linear sweep voltammetry data (Figure S13, Supporting Information). GaPtMnP/N-MWCNT exhibited the lowest overpotential (34 mV dec^{-1}) among the synthesized catalysts, implying that it was the most active toward the EOR.

Figure S14, Supporting Information, shows the CO stripping data of GaPtMnP/N-MWCNT, PtMnP/N-MWCNT, GaPtP/N-MWCNT, and PtP/N-MWCNT in a 0.3 M solution of H_2SO_4 under nitrogen atmosphere at a scan rate of 10 mV s^{-1} . To determine the electroactive surface area after CO stripping we calculated the ECSA_{CO} using the following equation:

$$\text{ECSA}_{\text{CO}} = \frac{Q_{\text{CO, des}}}{Q_{\text{CO, ox}}} \times 10^2 \quad (1)$$

Table 1. Electrochemical performances of Pt-based catalysts toward the EOR.

Catalysts	Electrolyte	Mass activity [$A \text{ mg}_{\text{Pt}}^{-1}$]	ECSA [$\text{m}^2 \text{ g}^{-1}$]	Specific activity [mA cm^{-2}]	Cycling life and active percentage	Ref.
Pt ₆₉ Rh ₈ Fe ₂₃ -PNS@MXene	1.0 M KOH + 1.0 M ethanol	3.407	46.4	7.3	72.8% (1000)	[69]
Pt-Rh NWs/C	0.1 M HClO ₄ + 0.5 M ethanol	1.55	74.6	2.08	51% (2000)	[70]
Pt ₂ Ir/C	0.5 M H ₂ SO ₄ + 1.0 M ethanol	1.02	72.9	1.40	≈80% (3000)	[71]
Pt ₆₉ Ni ₁₆ Rh ₁₅ NWs/C	0.1 M HClO ₄ + 0.5 M ethanol	1.53	68.9	2.3	–	[26]
Pt ₃ Sn NFs-L/C	0.1 M HClO ₄ + 0.5 M ethanol	1.46	69.5	2.10	55.0% (2000)	[8]
PtRh NP/GNS	1.0 M H ₂ SO ₄ + 1.0 M ethanol	1.0	48.7	2.8	86.0% (2000)	[72]
PtNi _{0.67} Pb _{0.26} NWs	0.1 M HClO ₄ + 0.2 M ethanol	0.83	77.4	1.07	66.5% (1000)	[73]
Pt ₃ Fe NWs	0.1 M HClO ₄ + 0.5 M ethanol	1.30	32.33	4.01	79.2% (1000)	[74]
Pt ₃ Sn–SnO ₂ /NG	1.0 M H ₂ SO ₄ + 1.0 M ethanol	1.365	–	≈1.8	60.2% (3000)	[75]
GaPtMnP/N-MWCNT	0.3 M H ₂ SO ₄ + 0.5 M ethanol	9.165	88.1	10.4	89.3% (3000)	This study

*NW = nanowire, NP = nanoparticle, NW = nanowire, NG = Nitrogen-doped graphene, GNS = graphene nanosheets, and NFs = nanofibers.

where $Q_{\text{CO, des}}$ is the electronic charge of CO desorption, (derived from Figure S14, Supporting Information), Q_{CO} is the theoretical charge required to oxidize a single layer of CO on Pt ($420 \mu\text{C cm}^{-2}$), and A is the amount of Pt ($\mu\text{g cm}^{-2}$) applied to the electrode.^[2] The EC_{SA} values obtained for GaPtMnP/N-MWCNT, GaPtP/N-MWCNT, PtMnP/N-MWCNT, and PtP/N-MWCNT were 65.03, 46.35, 35.62, and 29.37 $\text{m}^2 \text{ g}^{-1}$, respectively. Evidently, the GaPtMnP/N-MWCNT has a better CO stripping ability and can have larger active sites for further electrocatalytic reactions.

To characterize the reactant product obtained after the CV electrochemical tests of ethanol solutions of GaMnP/N-MWCNT and PtP/N-MWCNT catalysts, we performed their ex situ ¹H NMR spectroscopy and the results are shown in Figure S15, Supporting Information. The GaMnP/N-MWCNT catalyst solution exhibited residual ethanol content, which was confirmed from the triplet at 0.55, 0.56, and 0.58 ppm. The presence of acetic acid combined with methyl group was confirmed from the singlet at 2.75 ppm.^[78] The two peaks at 1.46 and 1.47 ppm corresponded to acetaldehyde.^[79] Similarly, for PtP/N-MWCNT, the residual ethanol content and the presence of acetic acid (with methyl group) was respectively confirmed from the triplet at 0.56, 0.57, and 0.59 ppm, and the singlet at 2.76 ppm. Furthermore, the two peaks at 1.47 and 1.49 ppm were attributed to acetaldehyde. For both GaMnP/N-MWCNT and PtP/N-MWCNT catalysts, the amount of acetaldehyde produced was found to be higher than that of acetic acid, which further confirms the lower overpotential of the electrocatalysts.^[80]

We further obtained ex situ FTIR spectra for GaPtMnP/N-MWCNT and PtP/N-MWCNT to identify the consumption of intermediate species and the final products of 0.5 M ethanol and 0.3 M H₂SO₄ solution, and the results are shown in Figure S16, Supporting Information. We observed a distinct number of absorption bands with an increase in the electrode potential. The absorption bands observed at 2343 and 2055 cm^{-1} are attributed to CO₂ formation and linearly bonded CO (CO_L) on the surface of the catalyst.^[81] The peaks centered at 1280, 1632, and 1715 cm^{-1} correspond to CH₃COO[−] formation, C=O stretching of adsorbed acetyl (CH₃CO*), and acetaldehyde (CH₃CHO).^[82] While the band at 1355 cm^{-1} correspond to the

double bond deformation of the –CH₃ symmetric of acetaldehyde.^[81] The peak at 1240 cm^{-1} is associated with the utilization of CH₃CHOH* and –O–Pt.^[83] Furthermore, the band at 1045 cm^{-1} corresponds to ethanol depletion.^[84] Notably, no CO adsorption was observed on the GaPtMnP/N-MWCNT surface with increasing potential. However, a small vivid CO peak at 2055 cm^{-1} was observed at the catalyst surface, in the potential range 0.3–0.7 V for PtP/N-MWCNT. The presence of CO on the catalyst surface could block the adsorption and oxidation of new cycles, thus decreasing the catalytic activity of the electrocatalysts. The GaPtMnP/N-MWCNT catalyst exhibited remarkable EOR activity than the PtP/N-MWCNT catalyst because of the weaker CO-adsorption on its surface and its superior ability to generate superficial oxides to carry on the oxidation process.

A schematic representation of the EOR mechanism on GaPtMnP/N-MWCNT is shown in Figure 5I. Basically, two reaction pathways are known for ethanol oxidation. In case of complete oxidation, CO₂ is produced; else, partial oxidation products such as CH₃CHO and CH₃COOH are formed (shown in Figure S17A, Supporting Information).^[80] However, CO₂ and CH₃COOH are the final products of the EOR because CH₃CHO can dissolve in the electrolyte solution and get re-adsorbed to the active sites of the catalysts, to be oxidized to CO₂ or CH₃COOH.^[85] As further oxidation of CH₃COOH is complicated and difficult, it subsequently dissolved in the electrolyte. During the complete oxidation of an ethanol molecule, 12 electrons are generated. In contrast, only two and four electrons are produced when partial oxidation leads to CH₃CHO and CH₃COOH, respectively. A detailed possible mechanism possible of ethanol oxidation by the GaPtMnP/N-MWCNT catalyst is discussed in the Supporting Information.

2.3. DEFC Single-Cell Tests

A typical operating setup for a DEFC is shown in Figure 6A. Generally, when CH₃CH₂OH interacts with an anodic electrocatalyst, H⁺ is oxidized and CO₂ is generated (CH₃CH₂OH + 3H₂O ↔ 2CO₂ + 12H⁺ + 12e[−], $E_a = 0.084 \text{ V}$). Subsequently, the proton (H⁺) passes through the solid polymer electrolyte

membrane and combines with the oxide ion on the cathode side, generating H_2O ($3\text{O}_2 + 12\text{H}^+ + 12\text{e}^- \leftrightarrow 6\text{H}_2\text{O}$, $E_c = 1.229\text{ V}$). This overall reaction ($\text{CH}_3\text{CH}_2\text{OH} + 3\text{O}_2 \leftrightarrow 2\text{CO}_2 + 3\text{H}_2\text{O}$, $E = 1.145\text{ V}$) can produce a cell voltage of 1.145 V. The single-cell I - V polarization curves for each catalyst were obtained at an operating temperature of $70\text{ }^\circ\text{C}$ and are shown in Figure 6B,C. The single cell based on GaPtMnP/N-MWCNT exhibited a maximum power density (MPD) of 86.64 mW cm^{-2} , which was almost 1.3, 1.6, 2.3, and 4.01 times higher than those of the cells based on GaPtP/N-MWCNT (67.28 mW cm^{-2}), PtMnP/N-MWCNT (55.67 mW cm^{-2}), PtP/N-MWCNT (37.94 mW cm^{-2}), and Pt/C (22.12 mW cm^{-2}), respectively. Table 2 explicitly compares the fuel cell performances of some recently reported Pt-based catalysts and that of the GaPtMnP/N-MWCNT catalyst prepared in this study. From the table, it is evident that GaPtMnP/N-MWCNT exhibited a better DEFC performance than the previously reported catalysts at $70\text{ }^\circ\text{C}$.

The stability of the DEFC with GaPtMnP/N-MWCNT as the anode was further examined in 2.0 M ethanol + 0.3 M H_2SO_4 as the anolyte and O_2 as the catholyte at $70\text{ }^\circ\text{C}$. Constant current loads of 60 and 30 mA cm^{-2} were applied to the GaPtMnP/N-MWCNT and PtP/N-MWCNT cells, respectively, as shown in Figure 6D. Initially, the cell voltage of GaPtMnP/N-MWCNT increased to 0.58 V within 2800 s , primarily due to the exposure of fresh active catalytic sites.^[5] Subsequently, the cell voltage decreased slightly (0.02 V) and remained stable for 50 h without major performance degradation. This indicates the high efficiency and durability of the cell, likely resulting from the rapid removal of unwanted adsorbing species, such as CO , CH_3COOH , and CH_3CHO , from the Pt active sites.^[11] The improved interaction between the current collector and the catalyst active sites also plays a crucial role in improving

the EOR kinetics of polymer electrolyte membrane fuel cells (PEMFCs).^[38] On the contrary, the PtP/N-MWCNT single cell showed voltage fluctuation that could arise from the release of gaseous products adsorbed on the catalyst surface, fuel cross-over, or the formation of violent bubbles or water flooding inside the membrane electrode assembly (MEA).^[11] The PtP/N-MWCNT catalyst also remained stable with a minimal decrease in the voltage from 0.47 to 0.37 V .

Generally, the multiple startup and shutdown processes in polymer electrolyte membrane fuel cells (PEMFCs) degrade their overall performance by ≈ 20 – 30% .^[86] This performance loss can be categorized as reversible or irreversible. The irreversible loss in the performance of single cells can be related to the dissolution of the catalyst nanoparticles, carbon corrosion, membrane shrinkage, and nanoparticle agglomeration.^[87] On the other hand, the formation of PtO, fuel impurities, water flooding, ionomer contamination, and adsorption of impurities at the catalyst surface lead to reversible losses, as they can be reversed.

To evaluate the durability of the GaPtMnP/N-MWCNT single cells, they were subjected to multiple startup and shutdown processes, as shown in Figure 7. No additional voltage and polarization loss was observed, and the MPD remained almost constant even after multiple startup and shutdown cycles. Additionally, the morphology of the GaPtMnP/N-MWCNT catalyst was examined after the multiple startup and shutdown cycle tests using TEM (Figure S18, Supporting Information). GaPtMnP/N-MWCNT retained its structural morphology, and the GaPtMnP alloy nanoparticles remained well-anchored on N-doped MWCNT. Furthermore, size growth or any significant nanoparticle agglomeration was not observed. This indicates that the GaPtMnP/N-MWCNT catalyst was highly durable and showed considerable potential for practical applications.

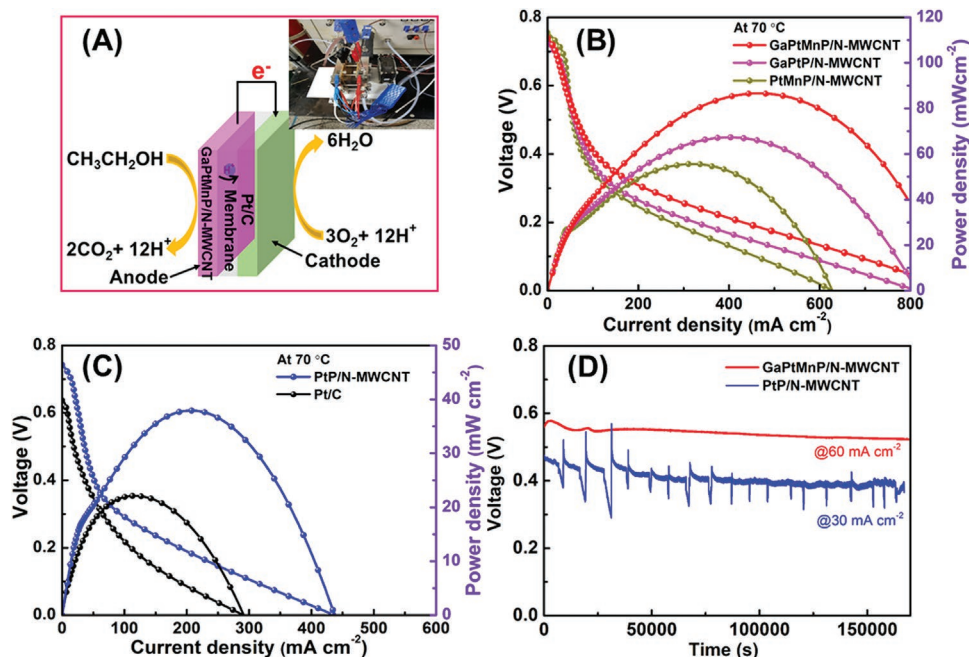


Figure 6. A) Schematic illustration and working principle of a DEFC; the inset is an image of our fuel cell module. I - V polarization curves of B) GaPtMnP/N-MWCNT, GaPtP/N-MWCNT, PtMnP/N-MWCNT, and C) PtP/N-MWCNT, Pt/C at $70\text{ }^\circ\text{C}$ in 2.0 M ethanol + 0.3 M H_2SO_4 (flow rate: 2 mL min^{-1}) and oxygen at the cathode side (flow rate: 200 sccm min^{-1}). D) Long-term stability test of the DEFCs at $70\text{ }^\circ\text{C}$ with a constant current load of 60 and 30 mA cm^{-2} for GaPtMnP/N-MWCNT and PtP/N-MWCNT, respectively.

Table 2. Electrochemical performances of recent Pt-based catalysts in DEFCs.

Anode	Cathode	Membrane	T °C	Fuel	MPD [mW cm ⁻²]	Ref.
Pt + SnO ₂ /C	Pt/C	Nafion 115	100	2.0 M ethanol +	58	[88]
G-Cys-Au@Pt	Pt/C	Nafion 115	80	1.0 M ethanol + 0.3 M H ₂ SO ₄	9.3	[89]
PtCu/Cu _{2-x} Se NWs	Pt/C	Nafion 117		2.0 M ethanol + 4.0 M H ₂ SO ₄	7.8	[83]
Pt-Ru-Re(1:1:0.5)/f-MWCNT	Pt/C (40 wt%)	Nafion 117	70	2.0 M ethanol +	19.15	[90]
Pt ₇₉ Sn ₁₅ Fe ₀₆	Pt/C	Nafion 117	80	2.0 M ethanol + 0.3 M H ₂ SO ₄	50	[91]
GaPtMnP/N-MWCNT	Pt/C (40 wt%)	Nafion 117	70	2.0 M ethanol + 0.3 M H ₂ SO ₄	86.64	This study

*MPD = Maximum power density, NW = Nanowire.

The alloy nanoparticles of GaPtMnP/N-MWCNT were found to be well-attached to the N-MWCNTs, and no growth in their particle sizes or agglomeration was observed after long-term operation under ethanol fuel, as illustrated schematically in Figure S17B, Supporting Information. This was further corroborated by the TEM and HAADF-STEM images shown in Figure S18, Supporting Information. In contrast, the PtP alloy in PtP/N-MWCNT exhibited agglomeration and Ostwald ripening after the long-term test, which was ascertained from their TEM and HAADF-STEM images (Figure S19, Supporting Information). This can be attributed to the PtP particle coarsening and dealloying, which occurs because of the high potential cycling as a function of the current–voltage profile.^[92,93] The HAADF-STEM image and line EDS of the PtMnP/N-MWCNT clearly depict the intact PtMnP alloy, as shown in Figure S20, Supporting Information. Similarly, the unblemished GaPtMnP alloy nanoparticles of the GaPtMnP/N-MWCNT catalyst were characterized by mapping and line EDS.

To further examine the structural stability of the alloy nanoparticles, XRD measurements of the employed GaPtMnP/N-MWCNT catalyst in a DEFC were performed, and the results are shown in Figure S21, Supporting Information. The GaPtMnP/N-MWCNT electrocatalyst was found to be stable even after a 500 h accelerated stress test along with multiple startup and shutdowns. However, we observed two new and low intensity diffraction peaks $\approx 53.96^\circ$ and 86.62° and correlated them with

the secondary phases of Mn₃Ga and Ga₃Pt₅. The peaks corresponding to the GaPtMnP alloy of the tested electrocatalyst was found to be sharper than those of their pristine counterparts. This implies that the GaPtMnP alloy achieved a higher degree of crystallinity, maintained a stable structure, and avoided dealloying of individual metals.^[94] Furthermore, the diffraction peak at 25.3° was attributed to the carbon paper that was used for casting the catalyst slurry; this carbon paper-supported catalyst was used as the anode electrode.

The outstanding catalytic performance of GaPtMnP/N-MWCNT toward the EOR can be attributed to the following factors. First, its ultrasmall spherical alloy nanoparticles with numerous surface atoms increased the atomic efficiency of Pt.^[95] Here, the use of ≈ 20 wt% Pt in GaPtMnP/N-MWCNT resulted in superior electrocatalytic activity compared with the use of 40 wt% Pt in commercial Pt/C, which reduces the overall cost of these anodic catalysts. Second, the introduction of Ga, Mn, and P isolated the Pt atoms at the surface and produced surface defects, which resulted in a high catalytic activity. Third, edge defects and vacancies generated from heteroatom N-doping in the carbon matrix (MWCNT) adsorbed more metal ions, which increased the capacity of the electrode, changed the surface structure, and improved the performance of the material. The introduction of nitrogen not only modulated the chemical reactivity and electronic conductivity of the carbon material, but was also beneficial for the removal of by-products and other unwanted species adsorbed on the catalyst surface.^[96,97]

The GaPtMnP/N-MWCNT and Pt/C-based single cells were further evaluated under hydrogen fuel to investigate their fuel flexibility. The current–voltage curves of the single cells are shown in Figure S22, Supporting Information. In the hydrogen–oxygen condition, the single cell with GaPtMnP/N-MWCNT delivered a remarkable current density of 600 mA cm^{-2} at 0.7 V. Furthermore, this cell exhibited an MPD of $512.29 \text{ mW cm}^{-2}$ at 70°C , which was ≈ 2.9 -fold higher compared with that of Pt/C ($176.18 \text{ mW cm}^{-2}$). The electrochemical performances of recently reported Pt-based anodic electrocatalysts under hydrogen fuel are summarized in Table ST5, Supporting Information. The GaPtMnP/N-MWCNT-based single cell exhibited excellent performance along with high durability and excellent fuel flexibility compared to the reported Pt-based catalytic cells. Thus, the presence of Ga-doped PtMnP alloy nanoparticles with a larger surface area along with uniform deposition on the N-MWCNT, which has a mesoporous structure and enhanced active-site density, makes GaPtMnP/N-MWCNT a potential anodic catalyst for DEFCs and hydrogen fuel cells.

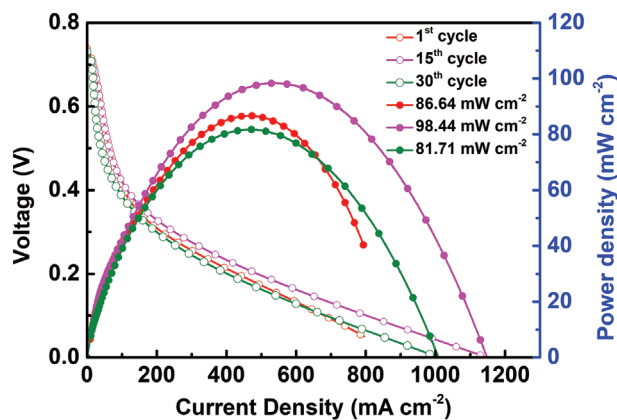


Figure 7. Polarization curves of a single cell based on the GaPtMnP/N-MWCNT anodic electrocatalyst after various startup and shutdown cycles under (0.3 M H₂SO₄ and 2.0 M ethanol solution) ethanol fuel at 70°C .

2.4. Atomic Structure Interpretation

Atomic-scale understanding is of great importance for designing highly efficient catalysts and controlling the reaction mechanism on their surfaces. We performed density functional theory (DFT) calculations to examine the observed experimental results for the structural characterization and electronic properties of the GaPtMnP catalyst. To build the GaPtMnP catalyst and provide an in-depth insight into the role of the dopant atoms (P, Mn, and Ga), we considered three doped slabs: i) P-doped Pt(111); ii) MnP-doped Pt(111); and iii) GaMnP-doped Pt(111). We then systematically investigated their atomic and electronic structures using spin-polarized DFT calculations.

To model a P-doped Pt (111) slab, we first studied single-atom doping by replacing a Pt atom in the surface and subsurface layers of Pt(111) with a P atom. According to the total energy calculations, the slab with the P-dopant atom in the outermost layer was 0.62 eV lower in energy than the one with the dopant in the subsurface (second atomic) layer. Such a high energy difference indicates that the P-dopant atom is energetically favored in the outermost layer of the Pt(111) slab. We further investigated two P dopants in the Pt(111) slab; the concentration of the doped atoms was $\approx 4\%$, which is consistent with that in the experiments ($\approx 4\text{--}5\%$). To explore the equilibrium atomic configuration of the dopant atoms in the slab, we systematically placed two P-dopant atoms at different spatial positions on the surface and subsurface layers. We noted that the 4×4 Pt(111) slab has six equivalent first-nearest neighbors (1NN), six equivalent second-nearest neighbors (2NN), and three equivalent third-nearest neighbors (3NN) sites for the two dopant atoms (Figure S23A, Supporting Information). The P-dopant atoms were initially placed at the 1NN, 2NN, and 3NN sites in the surface and subsurface layers of the Pt (111) slab. We observed that the P-dopant atoms, which were initially positioned at the 1NN site, moved to the 2NN site upon structural relaxation (Figure S23B, Supporting Information). This implies that P–P alloying in 1NN is not favorable on the surface and subsurface layers of the Pt(111) slab. Energetic screening revealed that the two P-dopant atoms in the Pt(111) slab preferred to be the outermost layer with 2NN configurations. The slab with P–P alloying in 2NN is referred to as “PtP(111)” (Figure S23B, Supporting Information).

Having established the equilibrium atomic configuration of the PtP(111) slab, we then performed spin-polarized DFT for Mn-doped PtP(111). To examine the equilibrium atomic configuration, a Pt atom on the surface and subsurface layers of the PtP(111) slab was substituted with a Mn atom. We found that the Mn-dopant atom energetically favors and tends to exist in the outermost layer, close to one of the dopant P atoms as 1NN on the surface by forming a P–Mn alloy (Figure S23D, Supporting Information). This indicates that the Mn–P bond formation is more favorable than the Pt–P formation, the reason being the large electronegativity difference between Mn (1.55) and P (2.19) compared to Pt (2.28) and P. As shown in **Figure 8C**, the slab with the P–P–Mn alloy in the outermost layer is referred to as “PtMnP(111),” and it was found to exhibit magnetic behavior with a magnetic moment of $3.4 \mu_B$, while the PtP(111) slab was nonmagnetic ($0 \mu_B$). Evidently, Mn doping spin-polarizes the PtP(111) slab.

To build the GaPtMnP catalyst, we investigated Ga doping of the PtMnP(111) slab. To this effect, a Pt atom in the surface and subsurface layers of the PtMnP(111) slab was substituted by a Ga atom. Total energy calculations revealed that the Ga atoms displayed no strong preference for the surface or subsurface layers of the slab (Figure S23E, Supporting Information). However, we observed that the Ga-doped atom was located far away from the Mn–P alloy in the slab. The energetically favorable positions of the Ga-doped atom in the surface and subsurface layers are presented in Figure 8D,E, and are referred to as “Ga(1L)PtMnP(111)” and “Ga(2L)PtMnP(111)”, respectively. The total magnetic moments of the Ga(1L)PtMnP(111) and Ga(2L)PtMnP(111) slabs were same as that of the PtMnP(111) slab, indicating that the magnetic moment in the GaPtMnP catalyst originates from the Mn atom.

2.5. Electronic Properties Investigation

To further provide in-depth insights into the effects of surface doping of P/Mn/Ga on the electronic structure of the catalyst, we analyzed the atom and orbital projected density of states (pDOS). The *d*-density of states for the Ga(1L)PtMnP(111) and Ga(2L)PtMnP(111) slabs are presented in Figure 8F. The results indicate that Mn doping in these slabs introduces magnetism by breaking the spin symmetry, which is reflected in the asymmetrical pDOS for spin-up and spin-down states near the Fermi level. Such spin-symmetry breaking of non-magnetic surfaces can improve the catalytic efficiency. As the magnetic moment of a metal surface significantly influences the reaction mechanism on the surface,^[98] Mn doping is a good strategy for inducing and manipulating magnetism in the GaPtMnP catalyst. Furthermore, the spin-up and spin-down states of Ga atoms in the Ga(1L)PtMnP(111) and Ga(2L)PtMnP(111) slabs are identical, indicating that the energy level near the Fermi level is not split. Thus, the Ga doping of the slabs did not destroy their spin symmetry.

Next, we analyzed the *d*-band center as an important parameter for the catalyst and found that it is dependent on the surface structure. Norskov and Hammer^[99] had demonstrated that the surface *d*-band center correlates with the binding strength between the catalyst and the reacting adsorbates. We calculated the *d*-band centers of the Pt(111), PtP(111), PtMnP(111), Ga(1L)PtMnP(111), and Ga(2L)PtMnP(111) slabs relative to the Fermi energy (E_F), and the results are illustrated in Figure 8G. We found that Mn doping in the PtP(111) slab led to an upward shift in the *d*-band center. Moreover, a higher *d*-band center was observed for Ga(1L)PtMnP(111) and Ga(2L)PtMnP(111) than for PtMnP(111), which can be explained by the higher electronegativity of Pt (2.28) than both Ga (1.81) and Mn (1.55). Thus, we revealed that Ga(1L)PtMnP has the highest *d*-band center compared to Pt(111) and PtMnP(111) slabs. This may be responsible for the better electrocatalytic activity of GaPtMnP/N-MWCNT toward ethanol oxidation compared with the other catalysts, which further concurs with the experimental electrochemical performance in this study. CO adsorption on the Pt surface can make an electrocatalyst inactive for the long-term electro-oxidation of ethanol molecules. However, CO adsorption can be minimized or eliminated by reducing the *d*-band center of Pt.

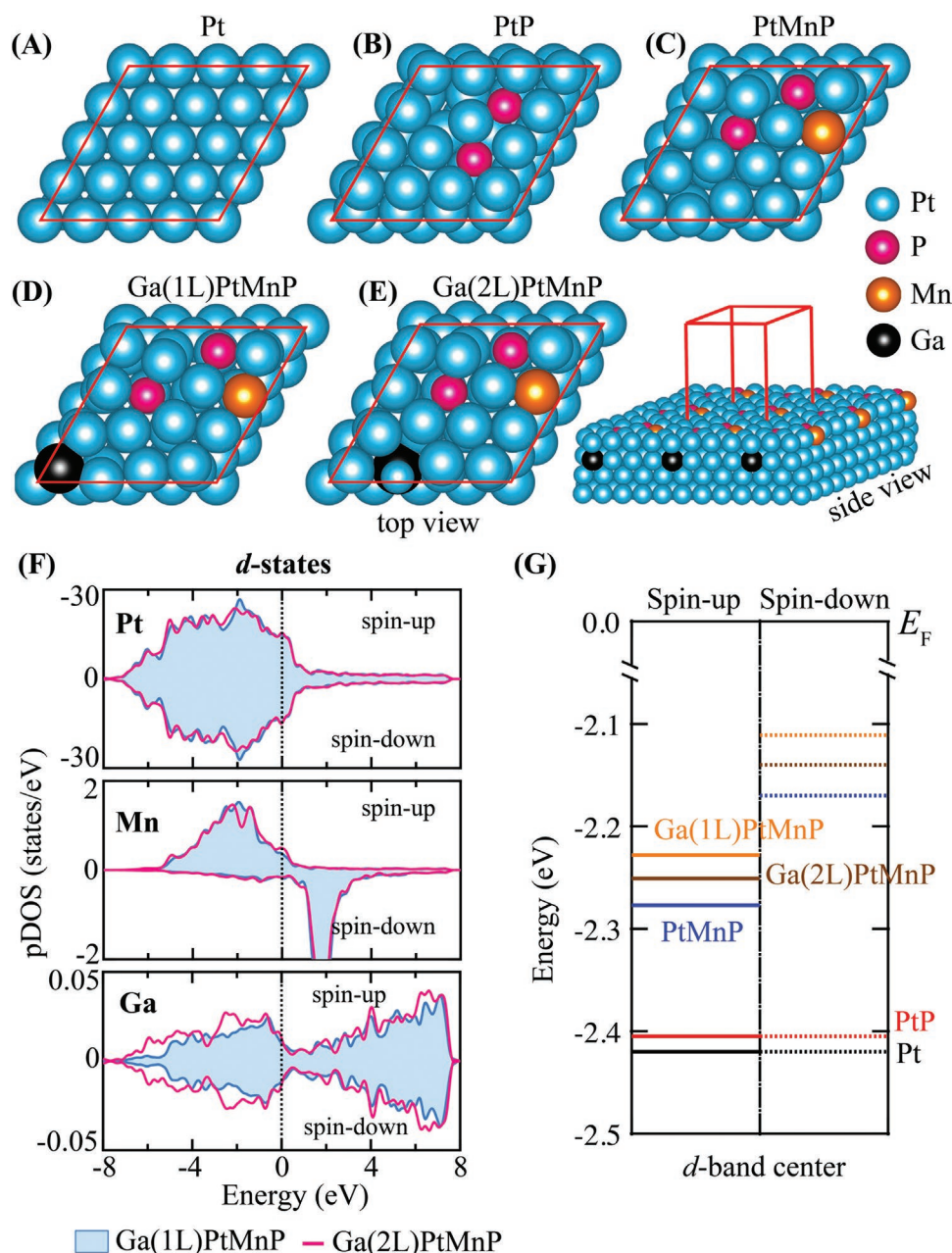


Figure 8. Atomic structure of A) Pt(111), B) PtP(111), C) PtMnP(111), D) Ga(1L)PtMnP(111), and E) Ga(2L)PtMnP(111) slabs. F) Projected density of states of Pt, Mn, and Ga atoms in the Ga(1L)PtMnP(111) and Ga(2L)PtMnP(111) slabs. G) The average d -band center of the presented slabs in (A–E). The Fermi energy (E_F) is set to 0 eV.

Owing to its reduced d -band center, CO adsorption is not significant in GaPtMnP/N-MWCNTs and does not contribute toward the degradation of this novel electrocatalyst.

3. Conclusion

GaPtMnP alloy nanoparticles were prepared and anchored onto N-MWCNTs to obtain an efficient electrocatalyst for the EOR. This catalyst exhibited an electrocatalytic activity superior to those of GaPtP/N-MWCNT, PtMnP/N-MWCNT, PtP/N-MWCNT, and Pt/C in a half-cell reaction. Furthermore, a single

cell based on GaPtMnP/N-MWCNT delivered an approximately fourfold higher peak power density than a commercial Pt/C cell. Moreover, ultrasmall P-containing spherical alloy nanoparticles and the rich valence electrons of GaPtMnP/N-MWCNT prevented any further dissolution and aggregation of the metals within the alloy and also modified its electronic structure, leading to outstanding activity and durability. The N-doped MWCNTs also contributed to the enhancement of the overall performance of GaPtMnP/N-MWCNT. The maintenance of the MPD and stability during multiple startup–shutdown cycles is the salient and promising feature of the GaPtMnP/N-MWCNT cell. Thus, this study provides valuable insights for synthesizing

novel nanocomposite electrocatalysts with rational compositions, enhanced catalytic activity, stability, and long-term durability for energy conversion in DEFCs and hydrogen fuel cells.

4. Experimental Section

Synthesis of GaPtMnP/N-MWCNT Alloy Nanoparticles: The MWCNTs were treated and purified according to a protocol described elsewhere.¹⁴⁸ The synthesis of GaPtMnP/N-MWCNT involved a simple two-step process. First, 2 g of the treated MWCNTs was dispersed in 150 mL of ethylene glycol. Subsequently, 20 mL of ethylene diamine was added dropwise, and the resultant solution was stirred for 24 h. Next, this reaction mixture was transferred to a Teflon vessel and heated at 180 °C for 4 h. The product acquired from the hydrothermal step was washed several times with deionized (DI) water and ethanol, and dried. Thus, N-doped MWCNTs were successfully prepared and applied as a carbon support in the next step.

In the second step, 60 mg of the N-doped MWCNTs and 5 mg of polyvinylpyrrolidone (PVP) were immersed in 50 mL of ethylene glycol and the mixture was stirred vigorously. In a separate vessel, the P precursor was prepared, along with Ga, Pt, and Mn (in a stoichiometric ratio of 1:3:1), for synthesizing the GaMnP alloy. Manganese (II) chloride tetrahydrate ([MnCl₂·4H₂O], 30 mg), gallium (III) nitrate hydrate ([Ga(NO₃)₃·xH₂O], 31 mg), and sodium hypophosphite monohydrate ([NaH₂PO₂], 6 mg) were stirred in 15 mL DI water for 3 h. Next, the solution containing the precursor metals was added dropwise to the N-doped MWCNTs, followed by vigorous stirring for 4 h. The Pt metal precursor (67 mg of chloroplatinic acid hexahydrate [H₂PtCl₆·6H₂O] in 5 mL DI water) was then added dropwise, and the resulting solution was stirred for 12 h. Subsequently, 180 μL of hydrazine monohydrate was gently poured into the above solution, following which the reaction was sealed in a Teflon vessel and heated at 160 °C for 5 h. The resulting precipitate from this hydrothermal process was collected and washed with ethanol and ultrapure DI water several times, then dried and ground to a fine powder. This fine powder is termed GaPtMnP/N-MWCNT. A similar procedure was employed to prepare GaPtP/N-MWCNT (1:3 for Ga and Pt), PtMnP/N-MWCNTs (3:1 for Pt and Mn), and PtP/N-MWCNTs. In all the catalysts, the (precursor) doping of P was maintained at 5%. For the optimization of Pt in GaPtMnP/N-MWCNTs, we synthesized GaPtMnP/N-MWCNTs with two different ratios of Pt (1:2.4:1 and 1:2:1), and the results are discussed in the Supporting Information.

Characterization and Electrochemical Analysis: The surface morphologies and microstructures of the as-synthesized catalysts were examined using SEM (Hitachi S-4200, Japan) and TEM (Tecnai G2F30, USA and JEOL JEM-2100, Japan). The crystalline phase and unit cell of the catalysts were analyzed using X-ray diffraction (XRD; SmartLab, Rigaku, Japan) at 30 mA and 40 kV. Cu K α radiation with a wavelength of 0.154 nm was employed, and the diffractometer was operated at a scan rate of 3° min⁻¹ (2 θ = 10–90°). The surface oxidation states and chemical compositions of the catalysts were investigated using XPS (Thermo VG, UK); an Al K α micro-focused monochromator was used for the same. Nitrogen adsorption and desorption isotherm measurements (Micromeritics, ASAP-2020, USA) were performed at STP to determine the specific surface area of the catalyst using the Brunauer–Emmett–Teller (BET) method, pore size distribution using the Barrett–Joyner–Halenda (BJH) method, and pore volume. ICP-MS (7900, Agilent, USA) was used to quantify the elements in the electrocatalysts. Fourier-transform infrared spectroscopy (FTIR, Nicolet iS50, Thermo Fisher Scientific, South Korea) was used to identify the stretching and adsorption of the catalysts. Nuclear magnetic resonance spectroscopy (NMR, 500 MHz, Jeol, JNM-ECZ500R/S1, Japan) was performed on the liquid samples to characterize the organic compounds generated from ethanol oxidation. The theoretical approach and computational details of the electrocatalyst are provided in Supporting Information.

Electrocatalytic measurements were performed using a potentiostat/galvanostat electrochemical analyzer (VSP-300, Biologic-Science

Instruments, France) consisting of a three-electrode cell system. A Pt wire was used as the counter electrode, while Ag/AgCl and catalyst-coated glassy carbon were employed as the reference and working electrodes, respectively. Prior to coating the catalyst on the glassy carbon electrode, it was cleaned and polished to obtain a fine mirror finish surface. To prepare the catalyst ink, 8 mg of the as-prepared catalyst powder was dispersed in 580 μL of an isopropanol and Nafion 117 (5 wt%) solution and ultrasonicated for ≈20 min, blending the catalyst ink. This blended catalyst ink (≈3 μL) was cast onto the polished glassy carbon electrode surface, dried, and used as a working electrode. Cyclic voltammetry (CV) was performed to measure the electrochemical activities of the catalysts, in 0.3 M H₂SO₄ + 0.5 M ethanol solution under a N₂-saturated atmosphere. The current density was evaluated at a scan rate of 20 mV s⁻¹. Electrochemical impedance spectroscopy (EIS) measurements were calibrated at 25 °C and conducted in a frequency range of 100 kHz to 10 mHz, with a signal amplitude of 5 mV.

Single-Cell Fabrication for the DEFC Tests: A single cell encompassing the GaPtMnP/N-MWCNT anodic catalyst was tested using ethanol and hydrogen as fuels. The single cells had a geometric active surface area of 5 cm² and were analyzed in a standard fuel cell station system. The catalyst paste was prepared according to the following protocol. First, 400 mg of GaPtMnP/N-MWCNT powder was added to a solution containing isopropanol and Nafion 117 (9:1 ratio) and then homogeneously dispersed by ultrasonication, which provided a viscous catalyst paste. The obtained catalyst paste was hand-brushed onto the surface of hydrophobic carbon paper and dried. This catalyst-loaded carbon paper served as the anode. For the electrolyte, a commercial Nafion 117 membrane was immersed in 3.0 M sulfuric acid for 48 h and then washed with DI water and used as an active membrane separator. Commercial Pt/C (40% Pt) was used as the cathode material. Membrane electrode assembly (MEA) was achieved by applying a hot-press (at 110 °C) with a pressure of 1.36 × 10⁴ Pa for 1 min. The same procedure was followed to prepare the GaPtP/N-MWCNT, PtMnP/N-MWCNT, and PtP/N-MWCNT based single cells for the DEFC test. The assembled single cells were positioned between two conducting graphite plates with a uniform flow channel model that was 1 mm in diameter. The current density and voltage (*I*–*V*) polarization curves of the single cells were obtained using a fuel cell station (Scitech company, South Korea). The anode part of the single cell was continuously supplied with 2.0 M ethanol + 0.3 M sulfuric acid solution (flow rate: 2 mL min⁻¹), while the cathode face was exposed to pure oxygen (flow rate: 200 sccm) at 70 °C.

Supporting Information

Supporting Information is available from the Wiley Online Library or from the author.

Acknowledgements

Y.S.Y., P.B., and M.E.K. contributed equally to this work. This research was conducted by the Korea Energy Technology Evaluation and Planning (KETEP) grant (2021400000690, GCU-AU next-generation fuel cell development project) and the National Research Foundation (NRF) grant (No. NRF-2019M2D1A1079208).

Conflict of Interest

The authors declare no conflict of interest.

Data Availability Statement

The data that support the findings of this study are available from the corresponding author upon reasonable request.

Keywords

alloy nanoparticles, electrocatalyst, ethanol oxidation, hydrogen, stability

Received: November 6, 2021

Revised: February 22, 2022

Published online:

- [1] X. Wu, J. He, M. Zhang, Z. Liu, S. Zhang, Y. Zhao, T. Li, F. Zhang, Z. Peng, N. Cheng, J. Zhang, X. Wen, Y. Xie, H. Tian, L. Cao, L. Bi, Y. Du, H. Zhang, J. Cheng, X. An, Y. Lei, H. Shen, J. Gan, X. Zu, S. Li, L. Qiao, *Nano Energy* **2020**, *67*, 104247.
- [2] W. J. Pech-Rodriguez, D. González-Quijano, G. Vargas-Gutierrezdia, C. Morais, T. W. Napporn, F. J. Rodríguez-Varela, *Appl. Catal. B* **2017**, *203*, 654.
- [3] A. M. L. Hidalgo, G. Magana, F. Rodriguez, A. D. L. Rodriguez, A. Sanchez, *Chem. Eng. J.* **2021**, *406*, 126829.
- [4] K. K. V. Diestra, L. P. S. Vandenberghe, L. A. Z. Torres, V. S. Nishida, A. Z. Filho, A. L. Woiciechowski, *Chem. Eng. J.* **2021**, *420*, 127708.
- [5] J. Guo, R. Chen, F. C. Zhu, S. G. Sun, H. M. Villullas, *Appl. Catal. B* **2018**, *224*, 602.
- [6] A. Kowal, M. Li, M. Shao, K. Sasaki, M. B. Vukmirovic, J. Zhang, N. S. Marinkovic, P. Liu, A. I. Frenkel, R. R. Adzic, *Nat. Mater.* **2009**, *8*, 325.
- [7] Z. Liang, L. Song, S. Deng, Y. Zhu, E. Stavitski, R. R. Adzic, J. Chen, J. X. Wang, *J. Am. Chem. Soc.* **2019**, *141*, 9629.
- [8] Y. Zhu, L. Bu, Q. Shao, X. Huang, *ACS Catal.* **2020**, *10*, 3455.
- [9] H. Xu, H. Shang, C. Wang, Y. Du, *Adv. Funct. Mater.* **2020**, *30*, 2000793.
- [10] W. Wang, X. Chen, X. Zhang, J. Ye, F. Xue, C. Zhen, X. Liao, H. Li, P. Li, M. Liu, Q. Kuang, Z. Xie, S. Xie, *Nano Energy* **2020**, *71*, 104623.
- [11] P. Basumatary, D. Konwar, Y. S. Yoon, *Appl. Catal. B* **2020**, *267*, 118724.
- [12] R. M. Altarawneh, T. M. Brueckner, B. Chen, P. G. Pickup, *J. Power Sources* **2018**, *400*, 369.
- [13] F. Wang, J. Qiao, H. Wu, J. Qi, W. Li, Z. Mao, Z. Wang, W. Sun, D. Rooney, K. Sun, *Chem. Eng. J.* **2017**, *317*, 623.
- [14] F. Gao, Y. Zhang, F. Ren, T. Song, Y. Du, *Nanoscale* **2020**, *12*, 12098.
- [15] L. Gao, X. Li, Z. Yao, H. Bai, Y. Lu, C. Ma, S. Lu, Z. Peng, J. Yang, A. Pan, H. Huang, *J. Am. Chem. Soc.* **2019**, *141*, 18083.
- [16] L. Huang, C. Y. Zheng, B. Shen, C. A. Mirkin, *Adv. Mater.* **2020**, *32*, 2002849.
- [17] J. Hu, C. Fang, X. Jiang, D. Zhang, Z. Cui, *Inorg. Chem. Front.* **2020**, *7*, 4377.
- [18] X. Ren, Y. Wang, A. Liu, Z. Zhang, Q. Lv, B. Liu, *J. Mater. Chem. A* **2020**, *8*, 24284.
- [19] Y. Kang, C. B. Murray, *J. Am. Chem. Soc.* **2010**, *132*, 7568.
- [20] J. R. Rodríguez, Y. V. Gómez, J. N. D. León, J. A. García, M. M. S. Paula, T. A. Zepeda, D. H. Galván, G. A. Núñez, *J. Mater. Res.* **2021**, *36*, 4216.
- [21] S. C. Lim, C. Y. Chan, K. T. Chen, H. Y. Tuan, *Electrochim. Acta* **2019**, *297*, 288.
- [22] Y. W. Lee, M. Im, J. W. Hong, S. W. Han, *ACS Appl. Mater. Interfaces* **2017**, *9*, 44018.
- [23] Y. Li, X. Li, H. S. Pillai, J. Lattimer, N. M. Adli, S. Karakalos, M. Chen, L. Guo, H. Xu, J. Yang, D. Su, H. Xin, G. Wu, *ACS Catal.* **2020**, *10*, 3945.
- [24] J. H. Lim, H. Shin, M. J. Kim, H. Lee, K. S. Lee, Y. K. Kwon, D. H. Song, S. K. Oh, H. Kim, E. A. Cho, *Nano Lett.* **2018**, *18*, 2450.
- [25] H. C. Kwon, Y. Park, J. Y. Park, R. Ryoo, H. Shin, M. Choi, *ACS Catal.* **2021**, *11*, 10767.
- [26] W. Zhang, Y. Yang, B. Huang, F. Lv, K. Wang, M. Luo, Y. Chao, Y. Li, Y. Sun, Z. Xu, Y. Qin, W. Yang, J. Zhou, Y. Du, D. Su, S. Guo, *Adv. Mater.* **2019**, *31*, 1805833.
- [27] M. Li, Z. Zhao, Z. Xia, Y. Yang, M. Luo, Y. Huang, Y. Sun, Y. Chao, W. Yang, W. Yang, Y. Yu, G. Lu, S. Guo, *ACS Catal.* **2020**, *10*, 3018.
- [28] T. Bauer, S. Maisel, D. Blaumeiser, J. Vecchiotti, N. Taccardi, P. Wasserscheid, A. Bonivardi, A. Görling, J. Libuda, *ACS Catal.* **2019**, *9*, 2842.
- [29] H. Lv, L. Sun, D. Xu, Y. Ma, B. Liu, *Appl. Catal. B* **2019**, *253*, 271.
- [30] M. Jiang, X. Li, W. Huang, M. Gan, L. Hu, H. He, H. Zhang, F. Xie, L. Ma, *Electrochim. Acta* **2019**, *323*, 134813.
- [31] H. Li, P. Wen, D. S. Itanze, Z. D. Hood, S. Adhikari, C. Lu, X. Ma, C. Dun, L. Jiang, D. L. Carrol, Y. Qiu, S. M. Geyer, *Nat. Commun.* **2020**, *11*, 3928.
- [32] L. Yang, G. Li, R. Ma, S. Hou, J. Chang, M. Ruan, W. Cai, Z. Jin, W. Xu, G. Wang, J. Ge, C. Liu, W. Xing, *Nano Res.* **2021**, *14*, 2853.
- [33] F. Wang, B. Fang, X. Yu, L. Feng, *ACS Appl. Mater. Interfaces* **2019**, *11*, 9496.
- [34] Z. Wang, H. Zhang, S. Yin, S. Liu, Z. Dai, Y. Xu, X. Li, L. Wang, H. Wang, *Sustainable Energy Fuels* **2020**, *4*, 2950.
- [35] X. Ji, B. Liu, X. Ren, X. Shi, A. M. Asiri, X. Sun, *ACS Sustainable Chem. Eng.* **2018**, *6*, 4499.
- [36] D. Shin, H. J. Kim, M. Kim, D. Shin, H. Kim, H. Song, S. Choi, *ACS Catal.* **2020**, *10*, 11665.
- [37] D. Lai, Z. Wang, Z. Wang, F. Gao, Q. Lu, *J. Power Sources* **2021**, *483*, 229137.
- [38] W. Li, Y. Li, H. Fu, G. Yang, Q. Zhang, S. Chen, F. Peng, *Chem. Eng. J.* **2020**, *381*, 122683.
- [39] R. Guo, W. Bi, K. Zhang, Y. Liu, C. Wang, Y. Zheng, M. Jin, *Chem. Mater.* **2019**, *31*, 8205.
- [40] Y. Chen, Z. Lai, X. Zhang, Z. Fan, Q. He, C. Tan, H. Zhang, *Nat. Rev. Chem.* **2020**, *4*, 243.
- [41] J. Liu, H. Zhang, M. Qiu, Z. Peng, M. K. H. Leung, W. F. Lin, J. Xuan, *J. Mater. Chem. A* **2020**, *8*, 2222.
- [42] B. W. Zhang, H. L. Yang, Y. X. Wang, S. X. Dou, H. K. Liu, *Adv. Energy Mater.* **2018**, *8*, 1703597.
- [43] Y. Wang, X. Zheng, D. Wang, *Nano Res.* **2021**, *15*, 1730.
- [44] S. Sui, X. Wang, X. Zhou, Y. Su, S. Riffat, C. J. Liu, *J. Mater. Chem. A* **2017**, *5*, 1808.
- [45] L. Castanheira, W. O. Silva, F. H. B. Lima, A. Crisci, L. Dubau, F. Millard, *ACS Catal.* **2015**, *5*, 2184.
- [46] R. A. M. Esfahani, E. B. Easton, *Appl. Catal. B* **2020**, *268*, 118743.
- [47] J. Zhang, S. Lu, Y. Xiang, S. P. Jiang, *ChemSusChem* **2020**, *13*, 2484.
- [48] P. Basumatary, D. Konwar, Y. S. Yoon, *Electrochim. Acta* **2018**, *261*, 78.
- [49] T. K. M. Amaral, G. O. Santos, P. S. C. Oliveira, N. J. Pires, V. G. Castro, G. G. Silva, A. M. L. Denadai, M. O. Alves, J. P. C. Trigueiro, R. L. Lavall, P. F. R. Ortega, *Chem. Eng. J.* **2020**, *388*, 124379.
- [50] J. C. Li, P. X. Hou, C. Liu, *Small* **2017**, *13*, 1702002.
- [51] H. Huang, L. Ma, C. S. Tiwary, Q. Jiang, K. Yin, W. Zhou, P. M. Ajayan, *Small* **2017**, *13*, 1603013.
- [52] B. N. Darshan, A. Kareem, T. Maiyalagan, V. E. Geo, *Int. J. Hydrogen Energy* **2021**, *46*, 13952.
- [53] R. Ragavan, A. Pandurangan, *New J. Chem.* **2017**, *41*, 11591.
- [54] D. Konwar, P. Basumatary, U. H. Lee, Y. S. Yoon, *J. Mater. Chem. A* **2021**, *9*, 10685.
- [55] P. Basumatary, U. H. Lee, D. Konwar, Y. S. Yoon, *Int. J. Hydrogen Energy* **2020**, *45*, 32770.
- [56] G. Ning, C. Xu, X. Zhu, R. Zhang, W. Qian, F. Wei, Z. Fan, J. Gao, *Carbon* **2013**, *56*, 38.
- [57] Y. Nakaya, J. Hirayama, S. Yamazoe, K. Shimizu, S. Furukawa, *Nat. Commun.* **2020**, *11*, 2838.
- [58] R. Shen, X. Wu, X. Li, J. Huang, S. Luo, J. Li, N. Qian, L. Ji, D. Yang, H. Zhang, *ChemistrySelect* **2021**, *6*, 3891.
- [59] Y. Li, C. Ou, J. Zhu, Z. Liu, J. Yu, W. Li, H. Zhang, Q. Zhang, Z. Guo, *Nano Lett.* **2020**, *20*, 2034.

- [60] X. Feng, Y. Bai, M. Liu, Y. Li, H. Yang, X. Wang, C. Wu, *Energy Environ. Sci.* **2021**, *14*, 2036.
- [61] K. Zhang, H. Wang, J. Qiu, J. Wu, H. Wang, J. Shao, Y. Deng, L. Yan, *Chem. Eng. J.* **2021**, *421*, 127786.
- [62] W. Gong, Z. Jiang, R. Wu, Y. Liu, L. Huang, N. Hu, P. Tsiakaras, P. K. Shen, *Appl. Catal. B* **2019**, *246*, 277.
- [63] R. Fang, H. Huang, J. Ji, M. He, Q. Feng, Y. Zhan, D. Y. C. Leung, *Chem. Eng. J.* **2018**, *334*, 2050.
- [64] T. T. Gebremariam, F. Chen, Q. Wang, J. Wang, Y. Liu, X. Wang, A. Qaseem, *ACS Appl. Energy Mater.* **2018**, *1*, 1612.
- [65] S. K. Singh, V. Kashyap, N. Manna, S. N. Bhange, R. Soni, R. Boukherroub, S. Szunerits, S. Kurungot, *ACS Catal.* **2017**, *7*, 6700.
- [66] K. Deng, Y. Xu, D. Yang, X. Qian, Z. Dai, Z. Wang, X. Li, L. Wang, H. Wang, *J. Mater. Chem. A* **2019**, *7*, 9791.
- [67] B. Peng, Y. Xu, K. Liu, X. Wang, F. M. Mulder, *ChemElectroChem* **2017**, *4*, 2140.
- [68] D. Konwar, P. Basumatary, S. P. Woo, Y. Lee, Y. S. Yoon, *Electrochim. Acta* **2018**, *290*, 142.
- [69] P. Wang, H. Cui, C. Wang, *Nano Energy* **2019**, *66*, 104196.
- [70] Y. Zhu, L. Bu, Q. Shao, X. Huang, *ACS Catal.* **2019**, *9*, 6607.
- [71] Y. Fang, D. Cao, Y. Shi, S. Guo, Q. Wang, G. Zhang, P. Cui, S. Cheng, *J. Phys. Chem. Lett.* **2021**, *12*, 6773.
- [72] Y. Shen, B. Gong, K. Xiao, L. Wang, *ACS Appl. Mater. Interfaces* **2017**, *9*, 3535.
- [73] N. Zhang, Y. Zhu, Q. Shao, X. Zhu, X. Huang, *J. Mater. Chem. A* **2017**, *5*, 18977.
- [74] Y. Zhang, F. Gao, T. Song, C. Wang, C. Chen, Y. Du, *Nanoscale* **2019**, *11*, 15561.
- [75] L. Wang, W. Wu, Z. Lei, T. Zeng, Y. Tan, N. Cheng, X. Sun, *J. Mater. Chem. A* **2020**, *8*, 592.
- [76] G. F. Li, M. Divinagracia, M. F. Labata, J. D. Ocon, P. Y. A. Chuang, *ACS Appl. Mater. Interfaces* **2019**, *11*, 33748.
- [77] Y. Qiu, J. Zhang, J. Jin, J. Sun, H. Tang, Q. Chen, Z. Zhang, W. Sun, G. Meng, Q. Xu, Y. Zhu, A. Han, L. Gu, D. Wang, Y. Li, *Nat. Commun.* **2021**, *12*, 5273.
- [78] A. Wang, D. Austin, A. Karmakar, G. M. Bernard, V. K. Michaelis, M. M. Yung, H. Zeng, H. Song, *ACS Catal.* **2017**, *7*, 3681.
- [79] R. M. Altarawneh, P. Majidi, P. G. Pickup, *J. Power Sources* **2017**, *351*, 106.
- [80] R. M. Altarawneh, *Energy Fuels* **2021**, *35*, 11594.
- [81] A. B. Delpuech, F. Maillard, M. Chatenet, P. Soudant, C. Cremers, *Appl. Catal. B* **2016**, *181*, 672.
- [82] K. Liu, W. Wang, P. Guo, J. Ye, Y. Wang, P. Li, Z. Lyu, Y. Geng, M. Liu, S. Liu, *Adv. Funct. Mater.* **2019**, *29*, 1806300.
- [83] H. Peng, J. Ren, Y. Wang, Y. Xiong, Q. Wang, Q. Li, X. Zhao, L. Zhan, L. Zheng, Y. Tang, Y. Lei, *Nano Energy* **2021**, *88*, 106307.
- [84] X. Yang, Z. Liang, S. Chen, M. Ma, Q. Wang, X. Tong, Q. Zhang, J. Ye, L. Gu, N. Yang, *Small* **2020**, *26*, 2004727.
- [85] G. Yang, Q. Zhang, H. Yu, F. Peng, *Particuology* **2021**, *58*, 169.
- [86] S. K. Babu, D. Spornjak, J. Dillet, A. Lamibrac, G. Maranzana, S. Didierjean, O. Lottin, R. L. Borup, R. Mukundan, *Appl. Energy* **2019**, *254*, 113659.
- [87] Q. Zhang, M. Schulze, P. Gazdzicki, K. A. Friedrich, *Appl. Energy* **2021**, *302*, 117490.
- [88] R. M. Antoniassi, J. C. M. Silva, A. O. Neto, E. V. Spinace, *Appl. Catal. B* **2017**, *218*, 91.
- [89] N. Seselj, C. Engelbrekt, Y. Ding, H. A. Hjuler, J. Ulstrup, J. Zhang, *Adv. Energy Mater.* **2018**, *8*, 1702609.
- [90] A. K. Choudhary, H. Pramanik, *Int. J. Hydrogen Energy* **2020**, *45*, 13300.
- [91] T. S. Almeida, A. R. V. Wassen, R. B. VanDover, A. R. D. Andrade, H. D. Abruna, *J. Power Sources* **2015**, *284*, 623.
- [92] M. C. Smith, J. A. Gilbert, J. R. Mawdsley, S. Seifert, D. J. Myers, *J. Am. Chem. Soc.* **2008**, *130*, 8112.
- [93] I. Khalakhan, M. Bogar, M. Vorokhta, P. Kúš, Y. Yakovlev, M. Dopita, D. J. S. Sandbeck, S. Cherevko, I. Matolínova, H. Amenitsch, *ACS Appl. Mater. Interfaces* **2020**, *12*, 17602.
- [94] M. R. Buck, R. E. Schaak, *Angew. Chem., Int. Ed.* **2013**, *52*, 6154.
- [95] E. Antolini, *Appl. Catal. B* **2016**, *181*, 298.
- [96] S. K. Singh, K. Takeyasu, J. Nakamura, *Adv. Mater.* **2019**, *31*, 1804297.
- [97] A. Sarapuu, E. K. Pöldsepp, M. Borghei, K. Tammeveski, *J. Mater. Chem. A* **2018**, *6*, 776.
- [98] J. Qian, Q. An, A. Fortunelli, R. J. Nielsen, W. A. Goddard, III, *J. Am. Chem. Soc.* **2018**, *140*, 6288.
- [99] B. Hammer, J. K. Nørskov, *Nature* **1995**, *376*, 238.